

Refined insight into $^{40}\text{Ar}/^{39}\text{Ar}$ progressive crushing technique from K–Cl–Ar correlations in fluid inclusions



Xiu-Juan Bai^a, Rong-Guo Hu^b, Ying-De Jiang^c, Xiao Liu^d, Bin Tang^d, Hua-Ning Qiu^{a,*}

^a Key Laboratory of Tectonics and Petroleum Resources (China University of Geosciences), Ministry of Education, Wuhan 430074, China

^b College of Earth Sciences, Guilin University of Technology, Guilin 541004, China

^c State Key Laboratory of Isotope Geochemistry, Guangzhou Institute of Geochemistry, Chinese Academy of Sciences, Guangzhou 510640, China

^d Institute of Nuclear Physics and Chemistry, China Academy of Engineering Physics, Mianyang 621900, China

ARTICLE INFO

Editor: Balz Kamber

Keywords:

$^{40}\text{Ar}/^{39}\text{Ar}$ crushing

Fluid inclusion

Mineralization age

Multi-component correlation

K–Cl–Ar 3D-diagram

ABSTRACT

Hydrothermal fluid activity associated with geological processes can now be dated by $^{40}\text{Ar}/^{39}\text{Ar}$ progressive crushing of minerals thanks to recent advances in high precision mass spectrometry. However, methods of data analysis and interpretation for these high-resolution measurements still need to be refined. In this study, we report further insights into using K–Cl–Ar diagrams as tools for interpreting ages of secondary and primary fluids from $^{40}\text{Ar}/^{39}\text{Ar}$ stepwise crushing experiments. Three paragenetic mineral pairs of muscovite and wolframites from a southern China tungsten deposit were investigated using the $^{40}\text{Ar}/^{39}\text{Ar}$ technique through laser incremental heating and progressive crushing of single minerals. Incremental heating analyses of muscovites yielded flat age spectra defining plateau ages of 156–153 Ma. Progressive crushing experiments of wolframites yielded anomalously old apparent ages due to excess ^{40}Ar . However, the apparent ages decline quickly after the initial steps and stabilize to form age plateaus of 156–153 Ma without excess ^{40}Ar . The plateau age steps interpreted as ages of gases derived from primary fluid inclusions (PFIs), yield well-defined isochrons with ages ranging from 157 to 153 Ma and initial $^{40}\text{Ar}/^{36}\text{Ar}$ values that are indistinguishable from the modern atmospheric value. Digitally created 2D- and 3D-diagrams of K–Cl–Ar correlations can easily reveal distribution trends and correlation planes from the crushing steps. Interpretations of these diagrams further reveal the ages of secondary fluid inclusions (SFIs) (87 to 83 Ma) and primary fluid inclusions (PFIs) (159 to 150 Ma). Raw data from SFIs degassed during the initial crushing steps form scatters on inverse isochron plots. However, 2D and 3D K–Cl–Ar diagrams yield SFI ages that agree with $^{40}\text{Ar}/^{39}\text{Ar}$ ages of K-feldspar veins cutting the tungsten ore bodies.

1. Introduction

$^{40}\text{Ar}/^{39}\text{Ar}$ dating method has a significant advantage over conventional K–Ar method (Turner, 1971b; Dalrymple et al., 1981; Roddick, 1983). One aspect is improved precision in age determination, where synchronous or nearly synchronous measurements of Ar isotope ratios of the same sample aliquot can be measured more precisely than ratios calculated from measurements of different sample aliquots for potassium and argon, respectively. Additionally, $^{40}\text{Ar}/^{39}\text{Ar}$ dating makes it feasible to date K-poor minerals, rocks and fluid inclusions. In recent years, $^{40}\text{Ar}/^{39}\text{Ar}$ progressive crushing techniques have been successfully applied to determine the ages of fluids associated with hydrothermal deposits (Qiu and Dai, 1989; Turner and Bannon, 1992; Turner and Wang, 1992; Qiu, 1996; Kendrick et al., 2001; Kendrick et al., 2006; Qiu and Jiang, 2007; Jiang et al., 2012; Bai et al., 2013; Liu et al., 2015), UHP metamorphism eclogites (Qiu and Wijbrans, 2006; Qiu and

Wijbrans, 2008; Hu et al., 2016), natural gas hydrocarbon accumulations (Yun et al., 2010; Liu et al., 2011; Qiu et al., 2011), as well as granites (Burgess and Parsons, 1994). Crushing techniques have also been effectively utilized to quantify noble gases ($^{39}\text{Ar}_\text{K}$ and $^{38}\text{Ar}_\text{Cl}$) produced by neutron irradiation of K and Cl, respectively (Sumino et al., 2011; Cartwright et al., 2013), providing information on fluid compositions and fluid sources (Kelley et al., 1986; Turner and Bannon, 1992; Kendrick et al., 2001; Kendrick et al., 2006). $^{40}\text{Ar}/^{39}\text{Ar}$ progressive crushing technique has become very important and irreplaceable in dating and tracing various geofluids.

Apart from the key $^{39}\text{K}(\text{n,p})^{39}\text{Ar}$ reaction, argon isotopes may be formed by neutron interactions with isotopes of calcium, potassium, argon, and chlorine (Merrihue and Turner, 1966; Mitchell, 1968; Berger and York, 1970; Turner, 1971b).

Mitchell (1968) recognized that activation of chlorine isotopes ^{35}Cl and ^{37}Cl would yield ^{36}Ar and ^{38}Ar during neutron irradiation, with

* Corresponding author.

E-mail address: huaningqiu@cug.edu.cn (H.-N. Qiu).

<https://doi.org/10.1016/j.chemgeo.2019.03.037>

Received 3 October 2018; Received in revised form 26 March 2019; Accepted 31 March 2019

Available online 01 April 2019

0009-2541/ © 2019 Elsevier B.V. All rights reserved.

subsequent β^- decay to produce ^{36}Ar and ^{38}Ar , respectively. The value of measuring ^{38}Ar generated from ^{37}Cl became widely recognized because it is a precise method to determine chlorine abundances, which is difficult to acquire through traditional acid digestion or *in situ* methods. In addition, useful correlations have been found between chlorine and excess or parentless ^{40}Ar components in some geological samples (McDougall and Harrison, 1999). Kelley et al. (1986) attempted to use $^{40}\text{Ar}/^{39}\text{Ar}$ technique to date fluid inclusions in quartz from veins associated with mineralization in two Paleozoic granites in England. They found that excess argon and chlorine were closely associated in the fluid inclusions. Subsequently, various studies confirmed a correlation between neutron-generated ^{38}Ar from ^{37}Cl and excess ^{40}Ar (Onstott et al., 1991; Böhlke and Irwin, 1992a; Böhlke and Irwin, 1992b; Burgess et al., 1992; Turner and Bannon, 1992; Turner and Wang, 1992; Harrison et al., 1993; Harrison et al., 1994; Qiu, 1996; Jiang et al., 2012; Bai et al., 2013). This correlation has been utilized to identify fluid sources.

Our preliminary study of wolframite $^{40}\text{Ar}/^{39}\text{Ar}$ crushing (Bai et al., 2013) showed the possibility to directly determine the mineralization ages of tin-tungsten deposits. To improve on those preliminary results, we have irradiated larger sample masses (from previous ~150 mg to now ~400 mg) and improved the determination of the irradiation J -values for this study. These new $^{40}\text{Ar}/^{39}\text{Ar}$ dating results are much better than the preliminary ones. Furthermore, utilizing a computer software (such as OriginLab Origin®), 3D-diagrams can be easily generated from measured data to better resolve argon isotopes derived from K and Cl during irradiation, obtain ages of SFIs and PFIs, identify sources of the fluids and deconvolve the excess ^{40}Ar from the radiogenic ^{40}Ar generated by *in situ* K decay.

2. Geological setting and samples

The South China Block consists of Yangtze Block to the west and the Cathaysian Block to the east. Both of these blocks amalgamated during the Neoproterozoic Sibao orogeny at ~1000 Ma (Liang et al., 2016). The Nanling Metallogenic Belt in the South China Block extends from south-eastern Guizhou, northern Guangxi, central-southern Hunan, northern Guangdong to southern Jiangxi, is famous for its world-class W–Sn polymetallic deposits that formed in the Jurassic (Chen et al., 2008; Liu and Yu, 2011; Hu and Zhou, 2012; Chen et al., 2013; Liu et al., 2014).

Our samples were collected from the Piaotang deposit in Dayu County, southern Jiangxi Province. The Piaotang Tungsten Deposit, located northeast of the Xihuashan granite (Fig. 1), is a large-scale quartz-vein-type tungsten polymetallic deposit in the Chongyi-Dayu-Shangyou cluster (He et al., 2010; Wang et al., 2010). The deposit has total metal reserves of 92,000 t of WO_3 (0.154% WO_3 ore grade) and 63,000 t of Sn (0.115% Sn ore grade), respectively, with byproducts of Cu, Zn and Ag (Mao et al., 2013; Zhang et al., 2017b). Its ore minerals mainly consist of wolframite, cassiterite, with some molybdenite, bismuthinite and chalcopyrite. Its gangue minerals include quartz, K-feldspar, fluorite and muscovite. The surrounding rocks are the Cambrian low-grade metamorphic sandstones, siltstones and slates.

Black wolframite is transparent to infrared radiation (Campbell et al., 1984; Campbell and Robinson-Cook, 1987). Using infrared microthermometry, fluid inclusions in wolframite were used to estimate their homogenization and ice-melting temperatures, from which fluid salinities could be obtained (Campbell and Robinson-Cook, 1987; Lüders, 1996; Lindaas et al., 2002). Infrared microthermometry of opaque minerals revealed that the temperatures of phase changes vary with the infrared light source intensity, resulting in overestimations of fluid salinities and underestimations of homogenization temperatures (Moritz, 2006).

Quartz-vein-type ore is most important in the Piaotang Tungsten Deposit, where grains of wolframite and quartz are usually larger than 10 mm in size. Some post-mineralization K-feldspar veins cut across wolframite quartz veins (Fig. 2). The wolframites contain abundant gas-

liquid two-phase fluid inclusions with circular, elongated, or negative-crystal shapes (Fig. 3). Based on the criteria of Goldstein and Reynolds (1994), primary fluid inclusions (PFIs) are best identified by their relationship with crystal growth zonations: they occur in growth zones or as isolated clusters in crystal cores. Secondary fluid inclusions commonly occur in planar arrays or along curved surfaces that cut across growth zonations. Primary and secondary fluid inclusions were identified within the wolframite studied here using the petrographic criteria above. The fluid inclusions within wolframites of Piaotang Tungsten Deposit can be divided into two groups based on their homogenization temperatures and salinities (Bai et al., 2013). Group I are fluid inclusions with homogenization temperatures to the liquid phase ranging from 300 to 360 °C and ice-melting temperatures from –3.0 to –5.2 °C, reflecting salinities from 5.0 to 8.0 wt% NaCl equivalent with an average of 6.0 wt%. Group II fluid inclusions have homogenization temperatures ranging from 200 to 280 °C and ice-melting temperatures from –0.3 to –4 °C. These temperatures correspond to salinities of 0.5–6.5 wt% NaCl with an average of 3.4 wt%. These homogenization and ice-melting temperatures of Group I are supported by the new data of Ni et al. (2015). Furthermore, estimated homogenization and ice-melting temperatures of both groups I and II also agree with data from wolframites in adjacent Yaogangxian Tungsten Deposit (Li et al., 2018).

3. Experimental methods

Wolframite and muscovite grains were hand-picked under a binocular microscope and cleaned in an ultrasonic bath using dilute nitric acid and distilled water. After cleaning, samples were dried in an oven at 120 °C. Wolframite samples of ca. 400 mg, with grain sizes of 30–60 mesh (0.50–0.25 mm), were irradiated for $^{40}\text{Ar}/^{39}\text{Ar}$ geochronology.

The Chinese standard samples for K–Ar dating of ZBH25 biotite was selected from the Fangshan granodiorite, Beijing. The mean concentrations of K and $^{40}\text{Ar}^*$ in the biotite are 7.6% and 1.813×10^{-9} mol/g, which correspond to a K–Ar age of 132.7 Ma. The biotite analyzed by $^{40}\text{Ar}/^{39}\text{Ar}$ step-heating experiment formed a flat age spectra with a plateau age of 132.7 Ma (Wang (1983), measured in the Australian National University using flux monitor GA-1550 biotite). The samples to be dated and monitor standards were packed in aluminum foil and copper foil, respectively, in thin cylinders (5–6 mm in diameter). They are placed inside aluminum (or quartz) tubes. Sealed aluminum (or quartz) tubes were loaded into an aluminum capsule packed with Cd-foil of 0.5 mm in thickness. The wolframite and muscovite samples were irradiated for ~50 h in the 49–2 reactor in Beijing. Correction factors of argon isotopes derived from Ca and K are $(^{39}\text{Ar}/^{37}\text{Ar})_{\text{Ca}} = 8.984 \times 10^{-4}$, $(^{36}\text{Ar}/^{37}\text{Ar})_{\text{Ca}} = 2.673 \times 10^{-4}$, and $(^{40}\text{Ar}/^{39}\text{Ar})_{\text{K}} = 5.97 \times 10^{-3}$, which are determined by measuring the relative production rates of these isotopes in co-irradiated pure calcium salt CaF_2 and potassium salt K_2SO_4 . The K-rich muscovite samples are analyzed by $^{40}\text{Ar}/^{39}\text{Ar}$ laser stepwise heating, and wolframite samples by $^{40}\text{Ar}/^{39}\text{Ar}$ progressive crushing. Fluid inclusions were extracted using a fully-automatic crushing apparatus that is directly connected with the purification line and mass spectrometer. In order to crush the sample as evenly as possible, two external electromagnets wrapped around the outside of the crusher tube are used to move the sample grains through pestle horizontal tapping. Detailed experiment procedures followed those described in Qiu and Jiang (2007) and Bai et al. (2013).

The released gases were first cleaned up in a newly designed gas purification system to remove moisture and organic gases released from the fluid inclusions (He et al., 2016). Two SAES NP10 Zr/Al getters further purify the gases at ~400 °C and room temperature respectively, generating noble gases with sufficient purity for argon isotope analyses in the mass spectrometer.

The argon isotopes of 09PT14Ms were analyzed using an ARGUS VI multi-collector mass spectrometer in the Key Laboratory of Tectonics and Petroleum Resources, Ministry of Education (Bai et al., 2018b). The

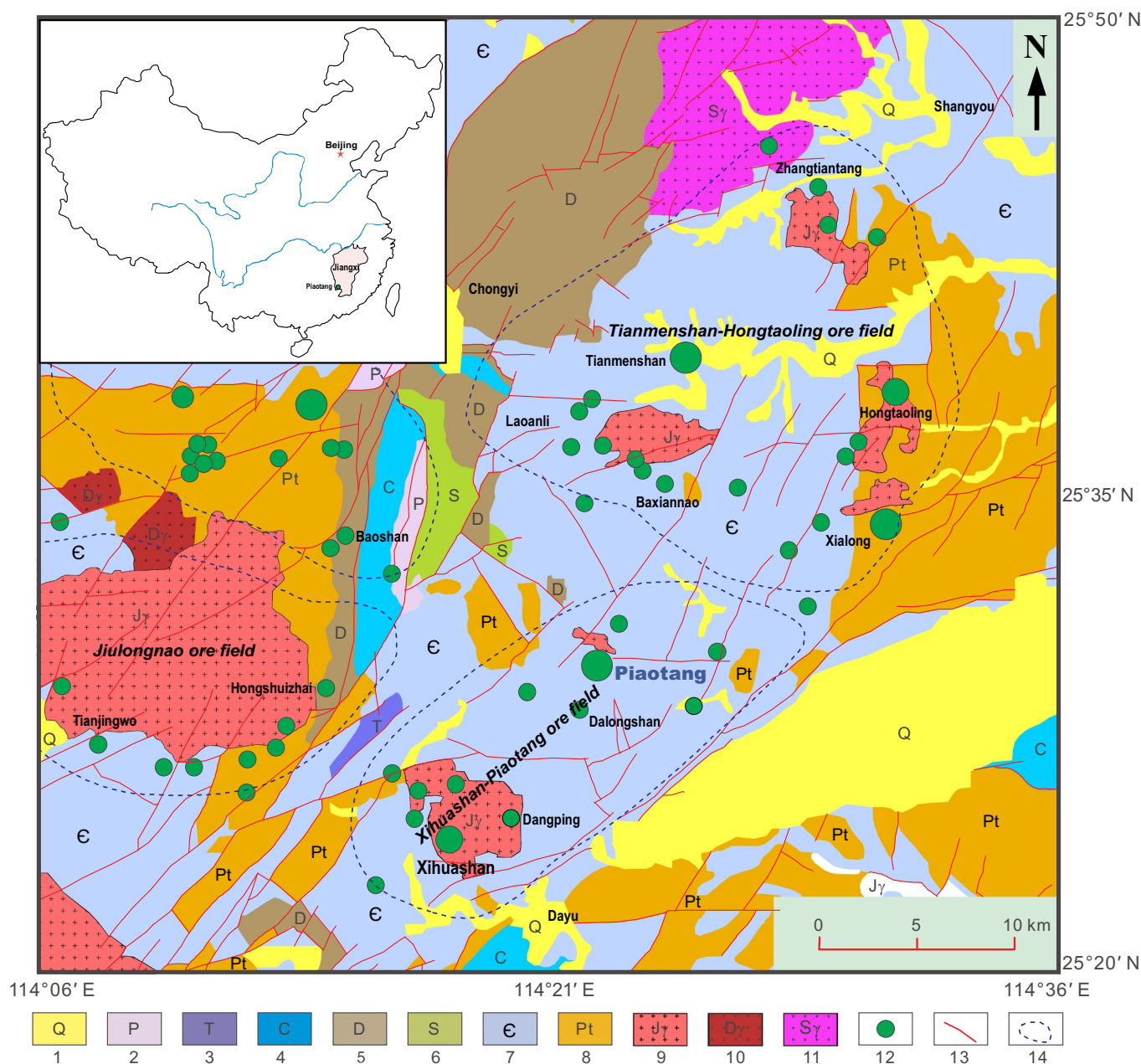


Fig. 1. Schematic geological map of the Chongyi-Dayu-Shangyou cluster in the southern Jiangxi tungsten district.

1-Quaternary; 2-Paleogene; 3-Carboniferous; 4-Devonian; 5-Silurian; 6-Ordovician; 7-Cambrian; 8-Proterozoic; 9-Jurassic granite; 10-Devonian granite; 11-Silurian granite; 12-Ore deposit; 13-Fault; 14-Ore field.

other samples were analyzed using a GVI-5400 noble gas mass spectrometer in the State Key Laboratory of Isotope Geochemistry, GIGCAS. The ARGUS VI collector array consists of five Faraday detectors equipped with resistors of $10^{11} \Omega$ (H2), $10^{12} \Omega$ (H1) and $10^{13} \Omega$ (Ax, L1 and L2), as well as a low mass CDD (compact discrete dynode) ion counting multiplier (in the L3 position). The collector array allows true simultaneous collection of five argon isotopes of ^{40}Ar – ^{36}Ar on H2–L2 (for big signal samples) or H1–L3 (for small signal samples), respectively.

4. Results

Three pairs of coexisting muscovites and wolframites were selected for comparison using the $^{40}\text{Ar}/^{39}\text{Ar}$ method. Potassium-rich mica samples were analyzed by laser stepwise heating and non-potassium wolframites by stepwise crushing *in vacuo*. $^{40}\text{Ar}/^{39}\text{Ar}$ data were

corrected, calculated and plotted using the ArArCALC software package (Koppers, 2002). The $^{40}\text{Ar}/^{39}\text{Ar}$ dating results are listed in Appendix A (Supplementary data of $^{40}\text{Ar}/^{39}\text{Ar}$ dating results). All reported analysis errors are 2σ in this paper.

All the muscovite samples dated by $^{40}\text{Ar}/^{39}\text{Ar}$ laser stepwise heating method yield flat age spectra (Fig. 4, solid red lines). The three muscovite plateau ages for samples 09PT14, 09PT46, and 09PT48 are 153.2 ± 1.5 , 155.4 ± 1.5 and 155.9 ± 1.5 Ma, respectively, which are concordant with their isochron ages of 153.2 ± 1.5 , 155.3 ± 1.6 and 155.8 ± 1.6 Ma.

All three wolframite samples dated by $^{40}\text{Ar}/^{39}\text{Ar}$ laser stepwise heating yield similar age spectra (Fig. 4, dark solid lines). Their apparent ages are unreasonably old for the first several steps, which then decrease drastically for the subsequent steps and finally form flat age plateaus for the final steps.

By excluding non-radiogenic ^{40}Ar with modern atmospheric

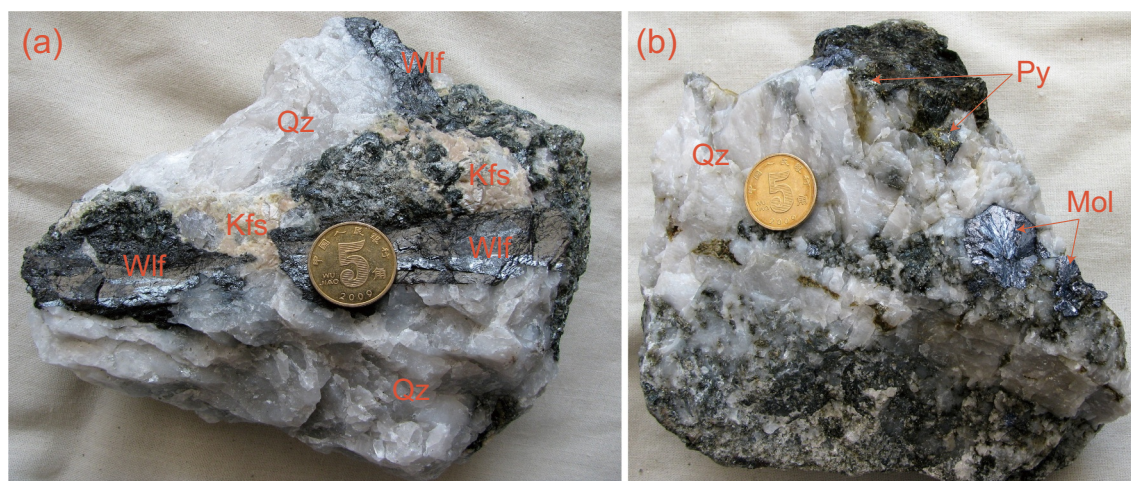


Fig. 2. Photo of a quartz-vein-type tungsten ores from Piaotang. Wlf: wolframite; Mol: molybdenite; Py: pyrite; Qz: quartz; Kfs: K-feldspar; Fl: fluorite.

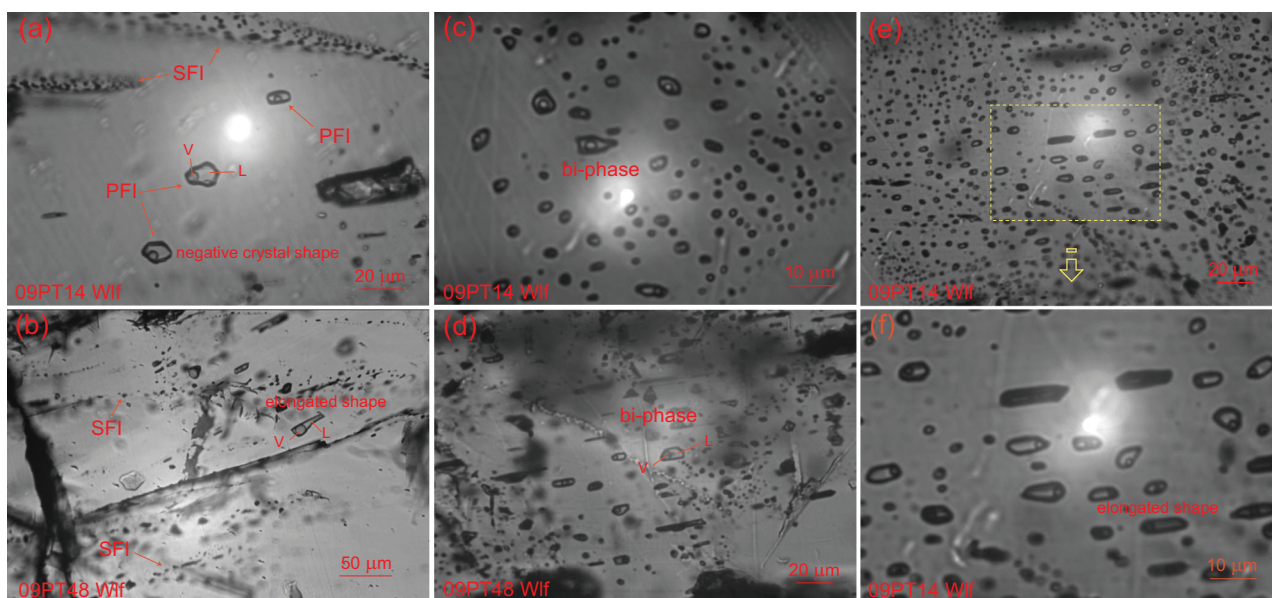


Fig. 3. Photomicrograph showing fluid inclusions in wolframite, taken with a ROLERA-XR infrared digital camera. (a) & (b) showing the secondary fluid inclusions distributing along microcracks; (c) to (f) showing plenty primary fluid inclusions in wolframite.

$^{40}\text{Ar}/^{36}\text{Ar}$ ratio of 295.5, stepwise crushed wolframite samples 09PT14, 09PT46, and 09PT48 yield abnormally old apparent ages (> 5 Ga) for the first three steps, which decrease drastically and form flat age plateaus for the final steps, yielding plateau ages of 152.6 ± 2.9 Ma (09PT14Wlf: steps 11–24, plateau $^{39}\text{Ar} = 56.9\%$), 154.7 ± 2.4 Ma (09PT46Wlf: steps 10–24, plateau $^{39}\text{Ar} = 70.3\%$) and 156.3 ± 3.1 Ma (09PT48Wlf, steps 9–25, plateau $^{39}\text{Ar} = 77.2\%$), respectively (Fig. 4a, b & c, dark solid lines). On inverse isochron plots of $^{36}\text{Ar}/^{40}\text{Ar}$ vs. $^{39}\text{Ar}/^{40}\text{Ar}$, the data points corresponding to the plateaus define isochrons with ages of 152.5 ± 5.9 Ma, 154.3 ± 4.6 Ma and 157.1 ± 5.7 Ma for samples 09PT14Wlf, 09PT46Wlf and 09PT48Wlf, respectively (Fig. 4d, e & f, blue lines). The initial $^{40}\text{Ar}/^{36}\text{Ar}$ ratios of all isochron lines are concordant and indistinguishable from atmospheric ratio of 295.5. It should be mentioned that most of the data for this study were obtained prior to 2013 on a GVI-5400[®] instrument at Guangzhou. For ease of comparison with the data published in Bai et al. (2013), we chose the atmospheric argon $^{40}\text{Ar}/^{36}\text{Ar}$ value of 295.5 and not the newly recommended value of 298.56 from Lee et al. (2006). However, the newer value has been used in our new laboratory in

Wuhan since 2015.

Data points from steps 4–8 of sample 09PT48Wlf also define an isochron with younger ages of 85.9 ± 16.9 Ma but a higher $^{40}\text{Ar}/^{36}\text{Ar}$ initial ratio of 330.2 ± 3.7 (Fig. 4f), indicating the presence of excess ^{40}Ar ($^{40}\text{Ar}_\text{E}$). Since wolframites contain trace amount of K, any initial argon component trapped in the fluid inclusions can easily affect their apparent ages. If this initial $^{40}\text{Ar}/^{36}\text{Ar}$ ratio is applied to exclude the non-radiogenic argon, the ages of steps 4–8 of 09PT48Wlf produce a weighted mean age of 85.7 ± 11.2 Ma, in agreement with their isochron age.

5. Discussion

5.1. Argon release pattern during progressive crushing

Gases released during progressive crushing have regular patterns. Qiu and Wijbrans (2008) proposed that the argon reservoirs and release patterns for extracting fluid inclusions can be measured by progressive crushing techniques. They interpreted that the gases in the early steps

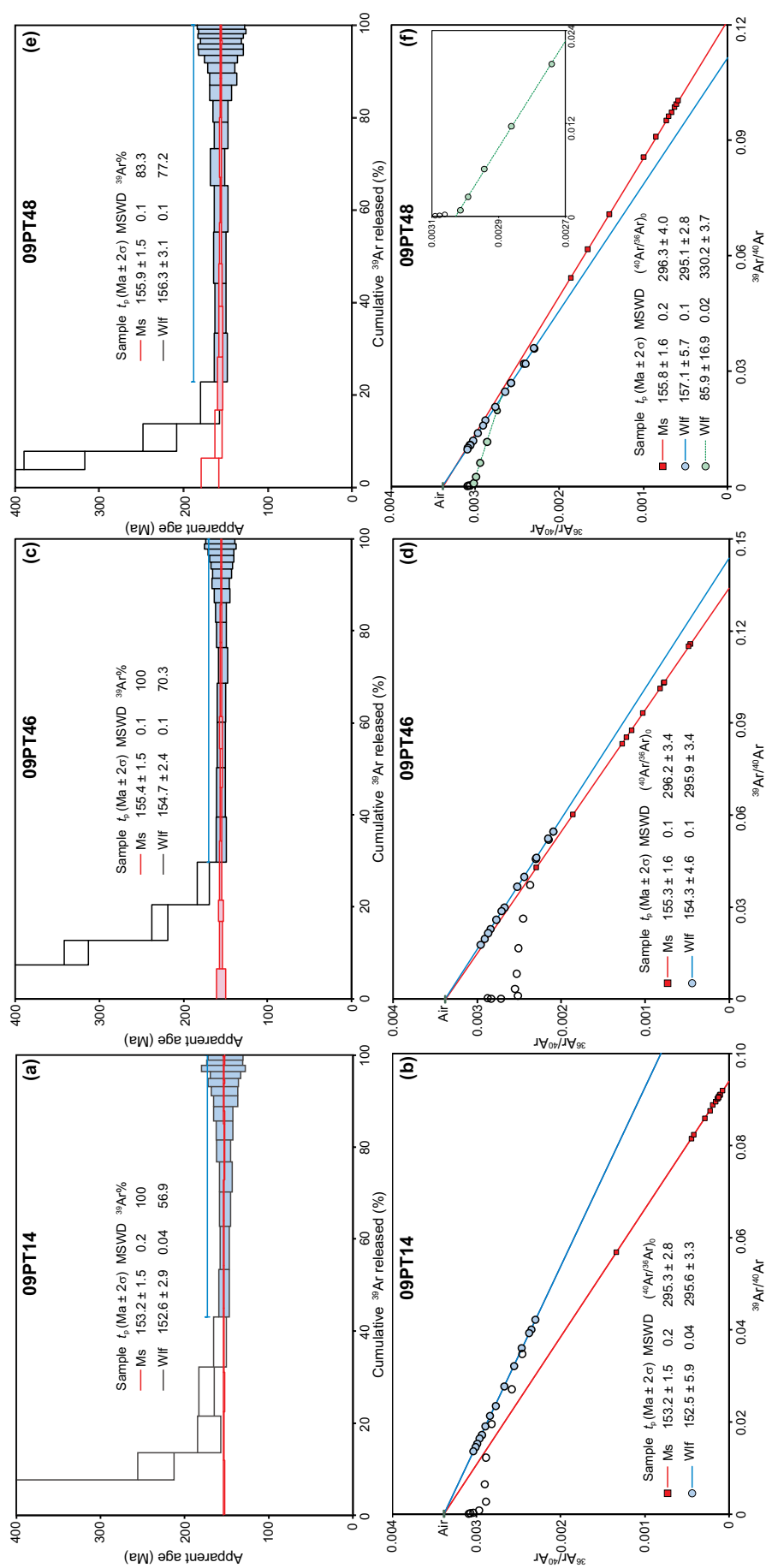


Fig. 4. $^{40}\text{Ar}/^{39}\text{Ar}$ age spectra and inverse isochrons of wolframites (light blue) by progressive crushing and their paragenetic muscovites (red) by laser heating. (For interpretation of the references to colour in this figure legend, the reader is referred to the web version of this article.)

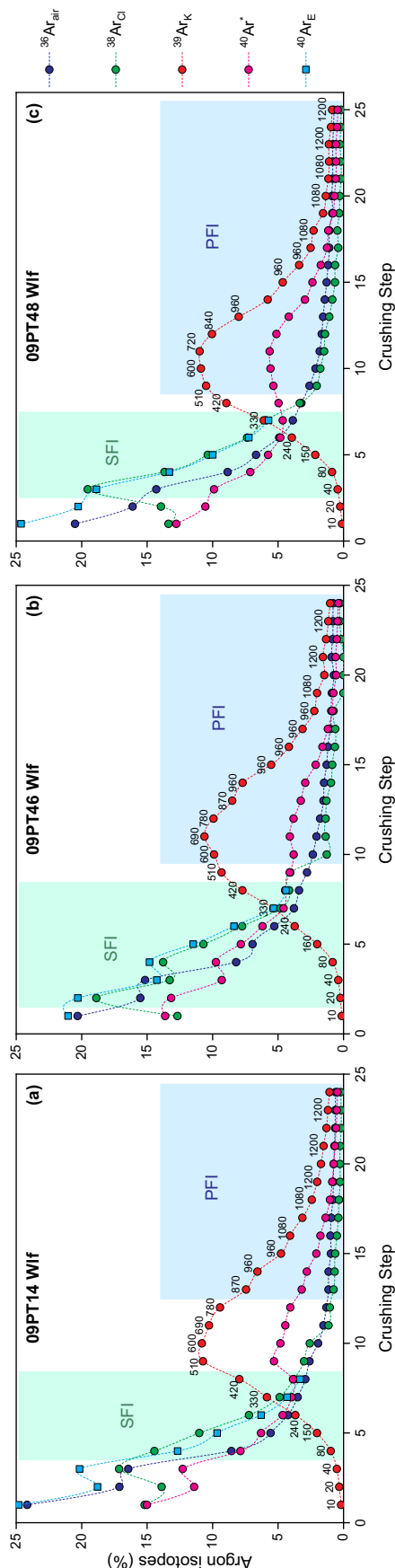


Fig. 5. Release patterns of argon isotopes during the progressive crushing experiments. The $^{40}\text{Ar}/^{39}\text{Ar}$ data are reduced by the ArArCALC software (Koppers, 2002). All the argon isotopes are routinely applied interference corrections for the interfering nuclear reactions with isotopes of Ca, K, Ar and Cl. $^{36}\text{Ar}_{\text{air}}$ – atmospheric ^{36}Ar ; $^{38}\text{Ar}_{\text{Cl}}$ – produced by chlorine during irradiation after the air correction; $^{39}\text{Ar}_{\text{K}}$ – produced in the key reaction on ^{39}K during irradiation; $^{40}\text{Ar}^*$ – after air correction, including the radiogenic ^{40}Ar from *in situ* decay of ^{40}K and the parentless excess ^{40}Ar ; $^{40}\text{Ar}_{\text{E}}$ – calculate corresponding to the SFIs ages, $^{40}\text{Ar}_{\text{E}} = ^{40}\text{Ar}_{\text{m}} - ^{40}\text{Ar}_{\text{air}} - ^{40}\text{Ar}_{\text{R}}$.

are preferentially released from the SFIs distributed along sealed fissure planes, which are more easily extracted by crushing. Gases released in the final steps are essentially all from small PFIs, mixed with atmospheric argon from the crusher. The secondary and primary fluid inclusions of the wolframites in this study are shown in Fig. 3 (a & b for SFIs and c–f for PFIs). Our new data agree with the proposed gas release pattern discussed above. In addition to the age spectra and data point distribution on inverse isochron plots (Fig. 4), these argon isotope release patterns can further expose differences between the SFIs and PFIs.

Patterns of $^{36}\text{Ar}_{\text{air}}$, $^{38}\text{Ar}_{\text{Cl}}$, $^{39}\text{Ar}_{\text{K}}$ and $^{40}\text{Ar}^*$ release for the three wolframites are illustrated in Fig. 5. The pestle drop numbers are marked on the $^{39}\text{Ar}_{\text{K}}$ curve. Here, $^{37}\text{Ar}_{\text{Ca}}$ is not shown due to very weak signals from the fluid inclusions. It should be noted that local radiation safety and transportation procedures led to long delays (up to 15 months) between irradiation and analysis, curtailing the ability to truthfully estimate $^{37}\text{Ar}_{\text{Ca}}$. The fluid inclusions studied here are low in Ca^{2+} (Liao, 2017) and therefore the 15-month time difference was not a problem. However, for inclusions with higher Ca, a more rapid turnaround would be necessary. After correcting for interfering ^{40}Ar produced during irradiation and atmospheric argon, the calculated $^{40}\text{Ar}^*$ includes radiogenic $^{40}\text{Ar}_{\text{R}}$ from *in situ* decay of ^{40}K and trapped excess $^{40}\text{Ar}_{\text{E}}$.

Samples 09PT14Wlf, 09PT46Wlf and 09PT48Wlf used in the progressive crushing experiments were about 400 mg in weight and underwent ~17,000 pestle drops in 24 or 25 crushing steps. Various argon reservoirs, including PFIs, SFIs, microcracks, crystal defects and mineral interfaces. Additionally, atmospheric argon trapped in the stainless steel crusher may be released during crushing. All argon isotope release patterns for the three wolframite samples are quite similar. Based on data point distributions on inverse isochron plots (Fig. 4) and K–Cl–Ar correlation plots (Fig. 6), the gas release process can be roughly grouped into three stages: dominantly SFIs in the initial steps; mixed gases from SFIs and PFIs in the medium steps; and dominantly PFIs in the final steps of the crushing procedures (Fig. 5).

For the initial steps, $^{36}\text{Ar}_{\text{air}}$, $^{38}\text{Ar}_{\text{Cl}}$, $^{40}\text{Ar}^*$ and $^{40}\text{Ar}_{\text{E}}$ generally start with their highest signals which then steadily decrease with additional crushing steps. $^{36}\text{Ar}_{\text{air}}$ represents atmospheric argon. Meanwhile $^{39}\text{Ar}_{\text{K}}$ signal generally increases stepwise from very low signals at first. The $^{40}\text{Ar}/^{39}\text{Ar}$ apparent ages of the wolframites are characterized with abnormally old apparent ages in the first two steps, which then decrease dramatically in steps 3–8. Large amounts of $^{40}\text{Ar}^*$ (23.2–26.7%), $^{38}\text{Ar}_{\text{Cl}}$ (27.3–31.5%) and $^{36}\text{Ar}_{\text{air}}$ (35.8–41.2%) are released in the initial two crushing steps with 30 pestle drops. However, < 0.5% $^{39}\text{Ar}_{\text{K}}$ is released at the same time, resulting in very high $^{40}\text{Ar}^*/^{39}\text{Ar}_{\text{K}}$ ratios and anomalously old apparent ages. The parentless $^{40}\text{Ar}^*$ are likely excess argon ($^{40}\text{Ar}_{\text{E}}$) released from SFIs that are distributed along microcracks, which are broken more easily during crushing than isolated PFIs. The decrease of $^{40}\text{Ar}^*/^{39}\text{Ar}_{\text{K}}$ ratios and apparent ages. Strong positive correlations exist between $^{40}\text{Ar}_{\text{E}}$ and $^{38}\text{Ar}_{\text{Cl}}$, with coefficients of $R^2 = 0.9998$ to 0.9999 (excluding the first few steps), which indicates that $^{40}\text{Ar}_{\text{E}}$ released from minerals that degassed at depth was trapped in SFIs in wolframites after tungsten mineralization. In summary, step-wise gas release with gentle force generates low $^{39}\text{Ar}_{\text{K}}$ and high $^{40}\text{Ar}_{\text{E}}$ during the initial steps, which are shown as the points close to the $^{36}\text{Ar}/^{40}\text{Ar}$ axis in the inverse isochron plots in Fig. 4. These steps correspond to abnormally old apparent ages, which could be attributed to $^{40}\text{Ar}_{\text{E}}$ trapped in microcracks after the formation of the secondary fluid inclusions. Additionally, $^{39}\text{Ar}_{\text{K}}$ increase from very low values in the first few steps to its peak in the medium steps, followed by slow decline in the final steps. This is consistent with the hypothesis that the larger PFIs contain most of the potassium.

During the final crushing steps, signals for all argon isotopes generally decline with progressive crushing, which demonstrates more uniform K–Cl–Ar distribution than those of initial and medium steps. These final steps are interpreted to represent gases released from small

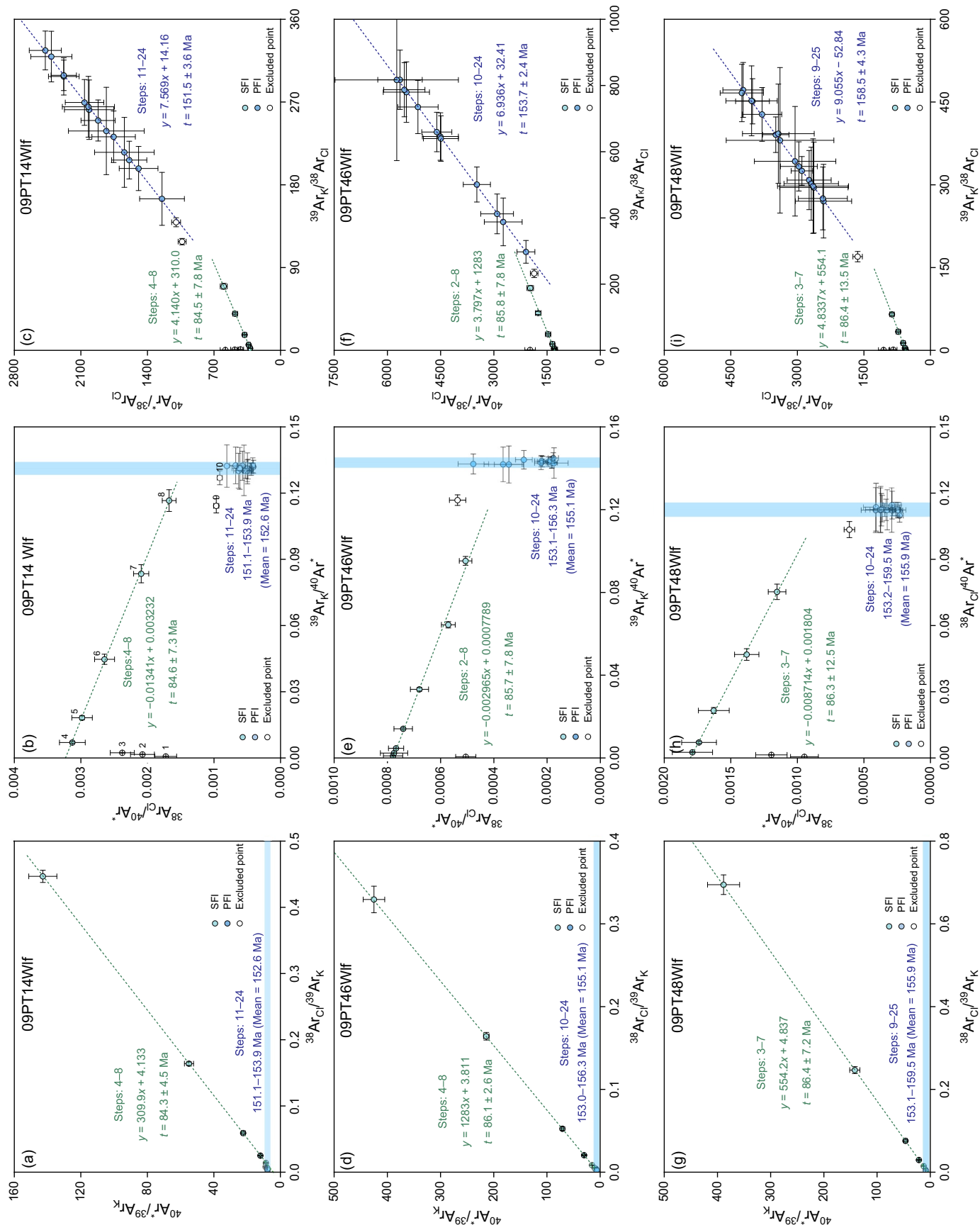


Fig. 6. Correlation diagrams of $^{38}\text{Ar}_{Cl}$, $^{39}\text{Ar}_K$ and $^{40}\text{Ar}^*$ of wolframites by progressive crushing. Argon isotopes are referred to the Fig. 5 captions.

(micron-size) PFIs, as indicated by the powder-size distribution observed by TEM analysis (Bai et al., 2013). The gases released in the final crushing steps are the most important because they usually define statistically significant isochrons and yield meaningful $^{40}\text{Ar}/^{39}\text{Ar}$ isochron ages that agree with ore-forming ages.

5.2. Correlations among $^{38}\text{Ar}_{\text{Cl}}$, $^{39}\text{Ar}_{\text{K}}$ and $^{40}\text{Ar}^*$

The SFIs are mainly sampled in the initial crushing steps. But the initial steps represent a mixture of gases from multiple reservoirs, including SFIs, some PFIs, and components that contain abundant excess ^{40}Ar . This gas release pattern makes it difficult to obtain one isochron line for the SFIs alone. Sometimes, when the SFIs are K-rich, gentle crushing may release gases from the SFIs only, without releasing measurable amount of gases from the PFIs. Two well-defined isochron lines that correspond to the SFIs and PFIs, respectively, were first obtained from hydrothermal sphalerites by slow increases of progressive gentle crushing numbers (Qiu and Jiang, 2007). Their ages were further verified by the K–Cl–Ar plots (Jiang et al., 2012). Similar cases of two isochrons (for the SFIs and PFIs, respectively) from one sample crushing experiment has sometimes been duplicated (Liu et al., 2011; Bai et al., 2018a). Unfortunately, excess argon is invariably present, making it difficult to produce an isochron from the early crushing steps, which typically sample gases from SFIs only. However, the plots based on K, Cl, and Ar isotope ratios (Fig. 6) yield distinct correlation lines and permit age calculations for both SFIs and PFIs (Jiang et al., 2012; Bai et al., 2013).

The argon isotopic ratios used for calculating correlations among $^{38}\text{Ar}_{\text{Cl}}$, $^{39}\text{Ar}_{\text{K}}$ and $^{40}\text{Ar}^*$ are listed in Table A1 of “Appendix A. Supplementary data of $^{40}\text{Ar}/^{39}\text{Ar}$ dating results”.

The apparent ages of the first several steps of wolframites are abnormally older than the ages of their contemporaneous muscovites, indicating the presence of excess ^{40}Ar in these steps. The initial steps in the wolframite crushing experiments contain excess argon ($^{40}\text{Ar}_{\text{E}}$), and they scatter on the inverse isochron diagrams (Fig. 4d, e & f, hollow circles). K-poor minerals (e.g. quartz, tourmaline, beryl, pyroxene and olivine) usually yield anomalously old K–Ar and $^{40}\text{Ar}/^{39}\text{Ar}$ ages because of excess ^{40}Ar . Fluid inclusions within K-poor minerals also contain excess ^{40}Ar (Rama et al., 1965; Kelley et al., 1986; Turner and Bannon, 1992; Turner et al., 1993; Kelley, 2002). The low potassium concentration and the presence of excess ^{40}Ar make it difficult to determine the ages of fluid inclusions by $^{40}\text{Ar}/^{39}\text{Ar}$ dating. However, previous crushing experiments have shown that secondary fluid inclusions containing $^{40}\text{Ar}_{\text{E}}$ can still yield meaningful isochron ages from the correlation diagrams of $^{40}\text{Ar}^*/^{39}\text{Ar}_{\text{K}}$ vs $^{38}\text{Ar}_{\text{Cl}}/^{39}\text{Ar}_{\text{K}}$, $^{38}\text{Ar}_{\text{Cl}}/^{40}\text{Ar}^*$ vs $^{39}\text{Ar}_{\text{K}}/^{40}\text{Ar}^*$ and $^{40}\text{Ar}^*/^{38}\text{Ar}_{\text{Cl}}$ vs $^{39}\text{Ar}_{\text{K}}/^{38}\text{Ar}_{\text{Cl}}$ (Turner and Bannon, 1992; Qiu, 1996; Kendrick et al., 2006; Jiang et al., 2012; Bai et al., 2013).

In $^{40}\text{Ar}^*/^{39}\text{Ar}_{\text{K}}$ vs $^{38}\text{Ar}_{\text{Cl}}/^{39}\text{Ar}_{\text{K}}$ space (Fig. 6a, d & g), several initial wolframite crushing steps show linear correlations with $^{40}\text{Ar}^*/^{39}\text{Ar}_{\text{K}}$ intercepts of 4.133 ± 0.2274 (1 σ) (09PT14Wlf, steps: 4–8), 3.811 ± 0.1172 (1 σ) (09PT46Wlf, steps: 2–8) and 4.837 ± 0.410 (1 σ) (09PT48Wlf, steps: 3–7), which correspond to ages of 84.3 ± 4.5 Ma, 86.1 ± 2.6 Ma and 86.4 ± 7.2 Ma, respectively. These are interpreted as the ages of the SFIs (Fig. 6a, d & g, green points and lines). In contrast, the final crushing steps (Fig. 6a, d & g, blue points) released extremely low $^{38}\text{Ar}_{\text{Cl}}$ without any correlation between $^{40}\text{Ar}^*/^{39}\text{Ar}_{\text{K}}$ and $^{38}\text{Ar}_{\text{Cl}}/^{39}\text{Ar}_{\text{K}}$, but with constant $^{40}\text{Ar}^*/^{39}\text{Ar}_{\text{K}}$ ratios close to the vertical axis. The average $^{40}\text{Ar}^*/^{39}\text{Ar}_{\text{K}}$ ratios correspond to ages of 152.6, 155.1 and 155.9 Ma, which are concordant with the isochron ages for the PFIs (Fig. 4d, e & f).

In $^{38}\text{Ar}_{\text{Cl}}/^{40}\text{Ar}^*$ vs $^{39}\text{Ar}_{\text{K}}/^{40}\text{Ar}^*$ space (Fig. 6b, e & h), the $^{38}\text{Ar}_{\text{Cl}}/^{40}\text{Ar}^*$ ratios gradually decrease with subsequent crushing steps, while the $^{39}\text{Ar}_{\text{K}}/^{40}\text{Ar}^*$ ratios ascend monotonically in the early steps until they reach constant values in the final steps. These ratios from the early crushing steps are inversely correlated. The intercepts of the

$^{39}\text{Ar}_{\text{K}}/^{40}\text{Ar}^*$ correlation line for the early steps are 0.2410 ± 0.02136 (1 σ) (09PT14Wlf, steps: 4–8), 0.2627 ± 0.02427 (1 σ) (09PT46Wlf, steps: 2–8) and 0.2070 ± 0.03074 (1 σ) (09PT48Wlf, steps: 3–7), which correspond to ages of 84.6 ± 7.3 Ma, 86.0 ± 7.8 Ma and 86.3 ± 12.5 Ma, respectively. These also represent SFI ages. The final steps have constant $^{39}\text{Ar}_{\text{K}}/^{40}\text{Ar}^*$ ratios but with wide $^{38}\text{Ar}_{\text{Cl}}/^{40}\text{Ar}^*$ ranges. The mean reciprocals of the $^{39}\text{Ar}_{\text{K}}/^{40}\text{Ar}^*$ ratios correspond to ages of 152.6, 155.1 and 155.9 Ma, which are concordant with the isochron ages for the PFIs (Fig. 4d, e & f).

On $^{40}\text{Ar}^*/^{38}\text{Ar}_{\text{Cl}}$ vs $^{39}\text{Ar}_{\text{K}}/^{38}\text{Ar}_{\text{Cl}}$ plots (Fig. 6c, f & i), both early and final steps yield good regression lines. The slopes of the correlation lines for the early steps, representing the $^{40}\text{Ar}^*/^{39}\text{Ar}_{\text{K}}$ ratios, are 4.140 ± 0.3903 (1 σ) (09PT14Wlf, steps: 4–8), 3.797 ± 0.3558 (1 σ) (09PT46Wlf, steps: 2–8) and 4.834 ± 0.7716 (1 σ) (09PT48Wlf, steps: 3–7), respectively. They correspond to ages of 84.5 ± 7.8 , 85.8 ± 7.8 and 86.4 ± 13.5 Ma. These ages are interpreted as the ages of the SFIs and they are concordant with the ages obtained for SFIs from the plot of $^{40}\text{Ar}^*/^{39}\text{Ar}_{\text{K}}$ vs $^{38}\text{Ar}_{\text{Cl}}/^{39}\text{Ar}_{\text{K}}$ (Fig. 6a, d & g) and $^{38}\text{Ar}_{\text{Cl}}/^{40}\text{Ar}^*$ vs $^{39}\text{Ar}_{\text{K}}/^{40}\text{Ar}^*$ (Fig. 6b, e & h). The final steps define lines with slopes of 7.569 ± 0.1861 (1 σ) (09PT14Wlf, steps: 11–24), 6.936 ± 0.1056 (1 σ) (09PT46Wlf, steps: 10–24) and 9.055 ± 0.2558 (1 σ) (09PT48Wlf, steps: 9–25), corresponding to ages of 151.5 ± 3.6 Ma, 153.7 ± 2.4 and 158.5 ± 4.3 Ma, respectively. These ages are indistinguishable from the isochron ages (Fig. 4d, e & f) and they are concordant with the ages obtained from the plots of $^{40}\text{Ar}^*/^{39}\text{Ar}_{\text{K}}$ vs $^{38}\text{Ar}_{\text{Cl}}/^{39}\text{Ar}_{\text{K}}$ (Fig. 6a, d & g) and $^{38}\text{Ar}_{\text{Cl}}/^{40}\text{Ar}^*$ vs $^{39}\text{Ar}_{\text{K}}/^{40}\text{Ar}^*$ (Fig. 6b, e & h) for PFIs.

5.3. Three-dimensional correlation diagrams

Early pioneer work applied multi-component correlation diagrams for irradiated samples (Turner, 1971a; Kelley et al., 1986; Turner, 1988). Now multi-component correlation diagrams can be better visualized through modern personal computers and software. In order to better understand K–Cl–Ar correlations and to get further constraints for SFI and PFI $^{40}\text{Ar}/^{39}\text{Ar}$ ages, two types of 3D correlation diagrams are shown in Fig. 7. These diagrams are based on the ratios of $(^{39}\text{Ar}_{\text{K}}/^{36}\text{Ar}_{\text{air}}) - (^{38}\text{Ar}_{\text{Cl}}/^{36}\text{Ar}_{\text{air}}) - (^{40}\text{Ar}/^{36}\text{Ar}_{\text{air}})$ and the ratios of $(^{39}\text{Ar}_{\text{K}}/^{40}\text{Ar}) - (^{38}\text{Ar}_{\text{Cl}}/^{40}\text{Ar}) - (^{36}\text{Ar}_{\text{air}}/^{40}\text{Ar})$ as the coordinate axes of X–Y–Z, respectively. Because the SFI data points are beneath the fitting planes of the PFIs on the plots of $(^{39}\text{Ar}_{\text{K}}/^{40}\text{Ar}) - (^{38}\text{Ar}_{\text{Cl}}/^{40}\text{Ar}) - (^{36}\text{Ar}_{\text{air}}/^{40}\text{Ar})$, more 3D diagrams are shown in Appendix B. To better view the correlation planes and data point distributions from different angles, the animation GIF pictures for the sample 09PT48Wlf (Fig. 7e and f) rotated for every 10° azimuth angle are uploaded as Appendix C with files named as ‘Fig. C7e.gif’ and ‘Fig. C7f.gif’ respectively.

Interesting features appear in the 3D-diagrams. Take Fig. 7a, c & e for example, the following observations can be made. Data point distribution trends with the crushing steps are shown as the red dot-dash lines. Because of the extremely low $^{39}\text{Ar}_{\text{K}}$, the initial steps fall near the plane of $(^{39}\text{Ar}_{\text{K}}/^{36}\text{Ar}_{\text{air}}) = 0$. ($^{40}\text{Ar}/^{36}\text{Ar}_{\text{air}}$) ratios increase with $(^{38}\text{Ar}_{\text{Cl}}/^{36}\text{Ar}_{\text{air}})$ ratios, generating a positive correlation between excess ^{40}Ar and chlorine. These data points do not yield an age. The K-bearing SFIs (green) define a correlation plane (light green). The K-bearing PFIs (blue) also define a correlation plane (light blue). A conventional isochron line of SFIs can be obtained from the intersection line of the SFIs correlation plane and the $(^{40}\text{Ar}_{\text{air}}/^{36}\text{Ar}_{\text{air}}) - (^{40}\text{Ar}_{\text{air}}/^{39}\text{Ar}_{\text{K}})$ plane, whose slope is applied to calculate SFIs age. (6) Similarly, the isochron line of PFIs from the intersection of the PFIs correlation plane and the $(^{40}\text{Ar}_{\text{air}}/^{36}\text{Ar}_{\text{air}}) - (^{40}\text{Ar}_{\text{air}}/^{39}\text{Ar}_{\text{K}})$ plane, fall on a statistically significant linear trend that corresponds to the age of the PFIs. Three wolframites yield SFI ages of 83.5, 86.0 and 86.4 Ma, and PFI ages of 149.5, 153.6 and 159.2 Ma. It is worth mentioning that both intercepts for SFI and PFI correlation planes with the Z-axis ($^{40}\text{Ar}/^{36}\text{Ar}_{\text{air}}$) are close to modern atmospheric argon ratio, indicating no excess ^{40}Ar ($^{40}\text{Ar}_{\text{E}}$) in the SFIs and the PFIs. However, the inverse isochron plots (Fig. 4d, e & f) show excess ^{40}Ar in the SFIs. In the 3D-diagrams, the $(^{40}\text{Ar}/^{36}\text{Ar}_{\text{air}})$ intercepts

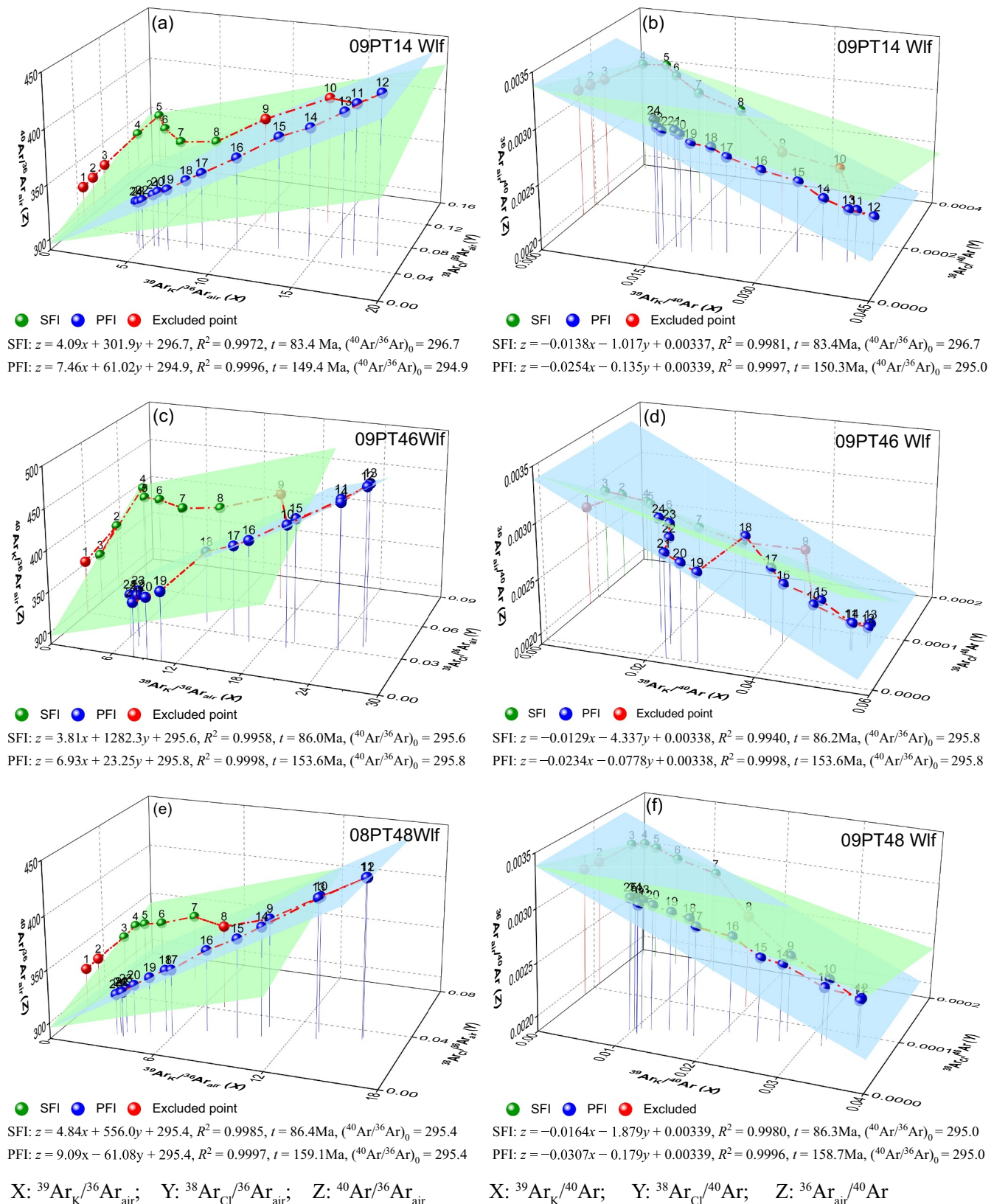


Fig. 7. Diagrammatic representation of the SFI (green) and PFI (blue) data as three-dimensional correlation planes. Because the SFI data points are beneath the fitting planes of the PFIs on the plots of $(^{39}\text{Ar}_K/^{40}\text{Ar}) - (^{38}\text{Ar}_{\text{Cl}}/^{40}\text{Ar}) - (^{36}\text{Ar}_{\text{air}}/^{40}\text{Ar})$ (right side), more 3D diagrams are shown in Appendix B. Animation GIF pictures for panels e and f rotated in every 10° azimuth angle are uploaded as Appendix C supplementary files named as 'Fig. C7e.gif' and 'Fig. C7f.gif'. Argon isotopes are referred to the Fig. 5 captions. (For interpretation of the references to colour in this figure legend, the reader is referred to the web version of this article.)

do not show excess ^{40}Ar because a chlorine correction has been applied.

In Fig. 7b, d & f, based on the ratios of $(^{39}\text{Ar}_\text{K}/^{40}\text{Ar}) - (^{38}\text{Ar}_\text{Cl}/^{40}\text{Ar}) - (^{36}\text{Ar}_\text{air}/^{40}\text{Ar})$, two correlation planes are also defined by data derived from SFIs and PFIs. The intercepts of the correlation planes on the Y-axis ($^{39}\text{Ar}_\text{K}/^{40}\text{Ar}$) are used to calculate SFI and PFI ages. Three wolframite samples yield SFI ages of 83.4, 86.2 and 86.3 Ma, and PFI ages of 150.3, 153.6 and 158.7 Ma. The initial $(^{40}\text{Ar}/^{36}\text{Ar})_0$ ratios for the three wolframite samples, calculated from the intercept reciprocals on the Z-axis ($^{36}\text{Ar}_\text{air}/^{40}\text{Ar}$) of SFI and PFI correlation planes, agree with modern atmospheric argon values.

Therefore, the 3D multi-component correlation diagrams provide an additional useful data reduction method to obtain the SFI and PFI ages for step-wise crushing experiments of irradiated hydrothermal minerals.

5.4. Age significance

The Piaotang Tungsten Deposit in southern Jiangxi Province has been dated by different geochronological methods, such as cassiterite U–Pb, zircon U–Pb and $^{40}\text{Ar}/^{39}\text{Ar}$ dating of paragenous muscovite, wolframite and cassiterite. Zircon U–Pb ages for the mineralization granite are 162–159 Ma (Zhang et al., 2009; He et al., 2010; Zhang et al., 2017b). The cassiterite samples, dated by both $^{40}\text{Ar}/^{39}\text{Ar}$ crushing and LA-ICP-MS U–Pb dating, yield a consistent age of 159 Ma (Bai et al., 2013; Zhang et al., 2017b). In this study, all muscovite samples from the ore veins yield very flat $^{40}\text{Ar}/^{39}\text{Ar}$ age spectra with concordant plateau ages and isochron ages ranging from 159 to 153 Ma (Bai et al., 2013; this study). All six wolframite samples also yield PFI ages ranging from 159 to 153 Ma by $^{40}\text{Ar}/^{39}\text{Ar}$ progressive crushing (Bai et al., 2013; this study). In summary, all the geochronological dates are concordant and consistent with the hypothesis that Piaotang mineralization occurred synchronously in the 160–150 Ma interval after granite intrusion, coeval with Late Jurassic large scale tin-tungsten mineralization in South China (Mao et al., 2004; Hua et al., 2005; Mao et al., 2006; Mao et al., 2007; Wu et al., 2010; Feng et al., 2011). *In situ* LA-ICP-MS zircon U–Pb ages of 134.4–132.9 Ma obtained from hydrothermal zircons from five wolframite-bearing-quartz-veins tungsten deposits in the Nanling Range (Wang et al., 2016) need further investigation.

Many small K-feldspar veins cut ore veins in Piaotang. Laser step heating analysis of K-feldspar samples yield flat age spectra with plateau ages of ~83 Ma (Bai et al., 2018a), indicating a wide hydrothermal fluid activity after the tungsten mineralization. This K-rich fluid certainly formed the secondary fluid inclusions in the ore minerals. On the inverse isochron plot, only one of the six wolframite samples (Bai et al., 2013; this study) yield an isochron line for the SFIs (Fig. 4f). It is very interesting that we can obtain significant SFIs ages from the 2D and 3D correlation diagrams based on the K–Cl–Ar components (Figs. 6–7). These SFIs ages are concordant with K-feldspar ages obtained by $^{40}\text{Ar}/^{39}\text{Ar}$ laser step heating.

5.5. Advantages of $^{40}\text{Ar}/^{39}\text{Ar}$ progressive crushing

With the development of analytical techniques and a new generation of mass spectrometers, many efforts have been made to directly date ore minerals: Re–Os dating of molybdenite (Du et al., 1993; McCandless et al., 1993; Suzuki et al., 1993), bitumen (Selby and Creaser, 2005; Gao et al., 2012) and pyrite (Morelli et al., 2004); U–Pb dating of uraninite (Richards et al., 1988; Fayek et al., 2002; Chipley et al., 2007; Suzuki and Kato, 2008; Cross et al., 2011) and cassiterite (Gulson and Jones, 1992; Yuan et al., 2008; Yuan et al., 2011; Xu et al., 2015; Li et al., 2016; Zhang et al., 2017a; Zhang et al., 2017b); Rb–Sr dating of sphalerite (Nakai et al., 1990; Brannon et al., 1992; Nakai et al., 1993; Christensen et al., 1995; Ostendorf et al., 2017; Guo et al., 2018; Xiong et al., 2018), pyrite (Yang and Zhou, 2001; Li et al., 2008; Zhao et al., 2013), and galkhaite (Tretbar et al., 2000); and Sm–Nd

dating of scheelite (Bell et al., 1989; Eichhorn et al., 1997; Kempe et al., 2001; Peng et al., 2003; Liu et al., 2007), chalcocopyrite (Maas et al., 1986), galena, sphalerite and pyrrhotite (Jiang et al., 2000). However, the concentrations of radioactive isotopes in ore minerals are commonly very low, and the range of isotopic ratios of the sample suite is usually not wide enough to define a good isochron line. Thus, it is often difficult to determine hydrothermal deposits using isochron methods that require solid materials.

Prior to the 1980s, fluid inclusions were not considered for dating. After the investigation of fluid inclusion geochronology by Shepherd and Darbyshire (1981), more studies were reported using Rb–Sr method (Changkakoti et al., 1988; Nakai et al., 1990; Nakai et al., 1993), followed by $^{40}\text{Ar}/^{39}\text{Ar}$ *in vacuo* crushing (Kelley et al., 1986; Qiu and Dai, 1989; Turner and Bannan, 1992; Qiu, 1996; Kendrick et al., 2001; Qiu et al., 2002).

SFIs are usually present in hydrothermal minerals. Mixing of SFIs and PFIs during sampling will cause the data points to scatter or result in a meaningless intermediate Rb–Sr isochron age. As discussed above, our progressive crushing technique has the potential to distinguish SFIs from PFIs. This finding is corroborated by Xiao et al. (2019) through combining QMS gas composition analysis with $^{40}\text{Ar}/^{39}\text{Ar}$ geochronology of fluid inclusions by progressive crushing. Their results indicated that the gases trapped in micro-cracks and large-sized vapor-rich secondary fluid inclusions, as well as large aqueous secondary fluid inclusions, were preferentially extracted in the initial crushing steps, and the dominant smaller primary fluid inclusions were released in the final crushing steps.

The ages of SFIs and PFIs are derived using both the $^{40}\text{Ar}/^{39}\text{Ar}$ inverse isochron plot and 2D- and 3D-plots based on K–Cl–Ar correlations. Furthermore, the gas mixing lines were demonstrated to correspond to the PFI ages in our recently published paper (Bai et al., 2018a). In other words, even if gas mixing of PFI and SFI components happens during progressive crushing, a geologically significant age might be still obtained from gas mixing lines.

We have widely applied the $^{40}\text{Ar}/^{39}\text{Ar}$ progressive crushing technique to date the ages of fluid inclusions in many non-potassium minerals from hydrothermal ore deposits (quartz, sphalerite, cassiterite and wolframite), ultra-high pressure metamorphic eclogites (garnet, omphacite, amphibole and quartz), tectonic quartz veins (quartz) and volcanic-rock-hosting natural gas reservoirs (quartz).

$^{40}\text{Ar}/^{39}\text{Ar}$ progressive crushing has many advantages over other methods:

- (1) An age spectrum and isochron line can be obtained by $^{40}\text{Ar}/^{39}\text{Ar}$ progressive crushing on just one sample. The plateau and isochron ages are usually concordant with each other, after applying a correction for excess ^{40}Ar based on the initial $(^{40}\text{Ar}/^{36}\text{Ar})_0$ ratio from the inverse isochron plot.
- (2) Many hydrothermal minerals with K-containing fluid inclusions are suitable for $^{40}\text{Ar}/^{39}\text{Ar}$ crushing, easily collected and separated, such as silicate, oxide, and sulphide minerals excluding Ca-rich ones. Therefore, $^{40}\text{Ar}/^{39}\text{Ar}$ progressive crushing technique can be widely applied to investigate timing of many geological events with fluid activities.
- (3) Inverse isochron plot based on $^{36}\text{Ar}/^{40}\text{Ar}$ vs $^{39}\text{Ar}/^{40}\text{Ar}$ can be used to obtain the true ages for samples, eliminating the effect of excess ^{40}Ar (if present).
- (4) SFIs and PFIs in a sample could be potentially separated by progressive crushing owing to the gaseous nature of Ar isotopes, which is much easier than solid isotope chronology systems. Furthermore, even if mixing of PFIs and SFIs occurs during progressive crushing, a gas mixing line still corresponds to a geologically meaningful age (Bai et al., 2018a).
- (5) Even if no inverse SFI $^{40}\text{Ar}/^{39}\text{Ar}$ isochron line is yielded, SFI and PFI ages may be still derived using 2D- and 3D-plots based on the K–Cl–Ar correlations, which provide additional useful approaches

to get meaningful age information for fluid activities.

5.6. Further experimental considerations

It is very important to obtain appropriate argon signals (^{39}Ar in particular) to yield a robust and precise $^{40}\text{Ar}/^{39}\text{Ar}$ age, requiring careful consideration of the most appropriate sample mass, potassium concentration and adequate irradiation J value.

5.6.1. Sample mass

In the pioneering studies between 2000 and 2006, about 30–50 mg of garnet, omphacite, sphalerite and other minerals were used for $^{40}\text{Ar}/^{39}\text{Ar}$ crushing, analyzed on the MAP-215-50 instrument at the VU University Amsterdam and the GVI-5400 instrument at the Guangzhou Institute of Geochemistry with electron multipliers. In order to reduce the air contribution from crushers and obtain better $^{40}\text{Ar}/^{39}\text{Ar}$ age data, larger sample masses of about 90–150 mg of quartz, cassiterite, wolframite and other minerals have been used since 2007 in the Guangzhou and Wuhan laboratories.

Quartz samples of ca 150 mg are appropriate for $^{40}\text{Ar}/^{39}\text{Ar}$ crushing. Considering the higher density of wolframite, the mass demand for wolframite is greater than that for quartz. In comparison with the preliminary results of ~150 mg wolframites (Bai et al., 2013), the $^{40}\text{Ar}/^{39}\text{Ar}$ dates of ~400 mg wolframites obtained in this study have been greatly improved.

5.6.2. Potassium concentration in fluid inclusions

The salinity of an individual fluid inclusion can traditionally be evaluated with the ice-melting temperature (Hall et al., 1988). Major and trace element compositions of individual fluid inclusion could be analyzed by LA-ICP-MS (Audétat et al., 1998; Günther et al., 1998; Heinrich et al., 1999), however, this technique is available only in a few laboratories. In practices, the milky quartz sample S-90Qw (Qiu, 1996) contains more potassium than the coexisting transparent quartz (unpublished data) from a tungsten ore. Fourteen dark sphalerite samples (Qiu and Jiang, 2007; Jiang et al., 2012) also have higher K concentrations than the seven brown sphalerite samples (unpublished data) from the Fankou Pb–Zn Deposit. These results are consistent with the finding of Audétat et al. (1998) that the early fluids had higher concentrations of most major and minor elements than the late fluids in the Yankee Lode tin deposit, Australia.

5.6.3. Neutron irradiation

To properly increase the ^{39}Ar production from ^{39}K by fast-neutrons in the 1.2–7 MeV energy range, optimization of irradiation parameters (Turner, 1971b; McDougall and Harrison, 1999) will improve the data quality of $^{40}\text{Ar}/^{39}\text{Ar}$ crushing.

Plots based on K–Cl–Ar correlations provide potential approaches to obtain the SFI and PFI ages, which is very important for the SFIs without an isochron line. $^{38}\text{Ar}_{\text{Cl}}$ production is directly proportional to the thermal-neutron fluence, however, Cd is usually used for common sample irradiation to shield the thermal-neutron fluence so that the $(^{40}\text{Ar}/^{39}\text{Ar})_{\text{K}}$ correction factor and the activity from other elements are reduced to acceptably low levels.

Quartz is the most important mineral available for $^{40}\text{Ar}/^{39}\text{Ar}$ crushing. Considering the trace potassium and low activity level of irradiated quartz samples, it would be a good idea to irradiate quartz samples separately from common samples with higher J values and without Cd-shielding in order to obtain more $^{39}\text{Ar}_{\text{K}}$ and $^{38}\text{Ar}_{\text{Cl}}$ for better analyses.

6. Conclusions

We conducted an integrated geochronological study to determine mineralization ages for the Piaotang Tungsten Deposit using $^{40}\text{Ar}/^{39}\text{Ar}$ stepwise laser heating and progressive crushing *in vacuo* techniques on

paragenetic muscovite and wolframite, respectively.

We found that large sample masses yielding appropriate argon levels are necessary for $^{40}\text{Ar}/^{39}\text{Ar}$ dating to obtain good age data. Relatively large masses of wolframite (~400 mg for each sample) resulted in much better $^{40}\text{Ar}/^{39}\text{Ar}$ dates than smaller mass fractions (~150 mg). In this study, all three wolframite samples yield concordant plateau and isochron ages of 157–153 Ma through progressive crushing, representing the ages of the primary fluid inclusions. These ages agree with those of co-existing muscovite crystals within 2–4% (2 σ). This study further confirms the feasibility of directly dating ore minerals in hydrothermal deposits using $^{40}\text{Ar}/^{39}\text{Ar}$ progressive crushing technique.

It is not easy to obtain an isochron for the SFIs on inverse isochron plot because gases are derived from multiple reservoirs and many contain excess ^{40}Ar . To crush samples gently with a few pestle drops in the initial steps has been shown to help removing some excess argon, avoiding PFIs release and generating meaningful SFI isochrons in subsequent several steps. 2D-diagrams of $(^{40}\text{Ar}^*/^{39}\text{Ar}_{\text{K}})$ vs $(^{38}\text{Ar}_{\text{Cl}}/^{39}\text{Ar}_{\text{K}})$, $(^{38}\text{Ar}_{\text{Cl}}/^{40}\text{Ar}^*)$ vs $(^{39}\text{Ar}_{\text{K}}/^{40}\text{Ar}^*)$ and $(^{40}\text{Ar}^*/^{38}\text{Ar}_{\text{Cl}})$ vs $(^{39}\text{Ar}_{\text{K}}/^{38}\text{Ar}_{\text{Cl}})$, and 3D-diagrams of $(^{39}\text{Ar}_{\text{K}}/^{36}\text{Ar}_{\text{air}}) - (^{38}\text{Ar}_{\text{Cl}}/^{36}\text{Ar}_{\text{air}}) - (^{40}\text{Ar}/^{36}\text{Ar}_{\text{air}})$ and $(^{39}\text{Ar}_{\text{K}}/^{40}\text{Ar}) - (^{38}\text{Ar}_{\text{Cl}}/^{40}\text{Ar}) - (^{36}\text{Ar}_{\text{air}}/^{40}\text{Ar})$, based on the K–Cl–Ar correlations in fluid inclusions, are shown to be useful approaches to obtain ages for SFIs and PFIs in wolframites. The PFI ages are comparable with ages obtained for coexisting muscovites, while the SFI ages match those obtained for late stage K-feldspar alteration.

All published geochronological dates indicate that the Piaotang ore deposit formed in the peak period of the Late Jurassic large-scale mineralization in the Nanling metallogenic belt, which agree with the ages that we have obtained through stepwise crushing. This suggests that many ore minerals like wolframite, cassiterite and sphalerite, as well as gangue minerals like quartz, could be directly dated by $^{40}\text{Ar}/^{39}\text{Ar}$ fluid inclusion progressive crushing. The $^{40}\text{Ar}/^{39}\text{Ar}$ progressive crushing technique can be widely applied to date fluid inclusions in many ore and gangue minerals with low potassium contents.

Acknowledgements

We are grateful to Prof. Balz Kamber and three anonymous reviewers for their constructive comments and suggestions, which greatly improved the manuscript. This study was financially supported by the National Natural Science Foundation of China (No.41873017, No.41630315, No.41503053 & No.41688103). A 100 Talents Program of the Chinese Academy of Sciences and a Guangdong Special Support Program to Y. D. Jiang is also acknowledged. We thank K. H. Lu for his kind helps during the fieldwork.

Appendix A. Supplementary data

Supplementary data to this article can be found online at <https://doi.org/10.1016/j.chemgeo.2019.03.037>.

References

- Audétat, A., Günther, D., Heinrich, C.A., 1998. Formation of a magmatic-hydrothermal ore deposit: insights with LA-ICP-MS analysis of fluid inclusions. *Science* 279 (5359), 2091–2094.
- Bai, X.J., Wang, M., Jiang, Y.D., Qiu, H.N., 2013. Direct dating of tin-tungsten mineralization of the Piaotang tungsten deposit, South China, by $^{40}\text{Ar}/^{39}\text{Ar}$ progressive crushing. *Geochim. Cosmochim. Acta* 114, 1–12.
- Bai, X.J., Jiang, Y.D., Hu, R.G., Gu, X.P., Qiu, H.N., 2018a. Revealing mineralization and subsequent hydrothermal events: insights from $^{40}\text{Ar}/^{39}\text{Ar}$ isochron and novel gas mixing lines of hydrothermal quartz by progressive crushing. *Chem. Geol.* 483, 332–341.
- Bai, X.J., Qiu, H.N., Liu, W.G., Mei, L.F., 2018b. Automatic $^{40}\text{Ar}/^{39}\text{Ar}$ dating techniques using multicollector ARGUS VI noble gas mass spectrometer with self-made peripheral apparatus. *J. Earth Sci.* 29 (2), 408–415.
- Bell, K., Anglin, C.D., Franklin, J.M., 1989. Sm–Nd and Rb–Sr isotope systematics of scheelites: possible implications for the age and genesis of vein-hosted gold deposits. *Geology* 17 (6), 500–504.
- Berger, G.W., York, D., 1970. Precision of the $^{40}\text{Ar}/^{39}\text{Ar}$ dating technique. *Earth Planet. Sci. Lett.* 9 (1), 39–44.

- Böhlke, J.K., Irwin, J.J., 1992a. Laser microprobe analyses of Cl, Br, I, and K in fluid inclusions: implications for sources of salinity in some ancient hydrothermal fluids. *Geochim. Cosmochim. Acta* 56 (1), 203–225.
- Böhlke, J.K., Irwin, J.J., 1992b. Laser microprobe analyses of noble-gas isotopes and halogens in fluid inclusions: analyses of microstandards and synthetic inclusions in quartz. *Geochim. Cosmochim. Acta* 56 (1), 187–201.
- Brannon, J.C., Podosek, F.A., McLimans, R.K., 1992. Alleghenian age of the Upper Mississippi Valley zinc lead deposit determined by Rb–Sr dating of sphalerite. *Nature* 356 (6369), 509–511.
- Burgess, R., Parsons, I., 1994. Argon and halogen geochemistry of hydrothermal fluids in the Loch Anort granite, Isle of Skye, Scotland. *Contrib. Mineral. Petrol.* 115 (3), 345–355.
- Burgess, R., Kelley, S.P., Parsons, I., Walker, F.D.L., Worden, R.H., 1992. ^{40}Ar – ^{39}Ar analysis of perthite microtextures and fluid inclusions in Alkali feldspars from the Klokken syenite, South Greenland. *Earth Planet. Sci. Lett.* 109 (1–2), 147–167.
- Campbell, A.R., Robinson-Cook, S., 1987. Infrared fluid inclusion microthermometry on coexisting wolframite and quartz. *Econ. Geol.* 82 (6), 1640–1645.
- Campbell, A.R., Hackbarth, C.J., Plumlee, G.S., Petersen, U., 1984. Internal features of ore minerals seen with the infrared microscope. *Econ. Geol.* 79 (6), 1387–1392.
- Cartwright, J.A., Gilmour, J.D., Burgess, R., 2013. Martian fluid and Martian weathering signatures identified in Nakhla, NWA 998 and MIL 03346 by halogen and noble gas analysis. *Geochim. Cosmochim. Acta* 105 (3), 255–293.
- Changkakoti, A., Gray, J., Krstic, D., Cumming, G.L., Morton, R.D., 1988. Determination of radiogenic isotopes (Rb/Sr, Sm/Nd and Pb/Pb) in fluid inclusion waters: an example from the Bluebell Pb–Zn deposit, British-Columbia, Canada. *Geochim. Cosmochim. Acta* 52 (5), 961–967.
- Chen, J., Lu, J.J., Chen, W.F., Wang, R.C., Ma, D.S., Zhu, J.C., Zhang, W.L., Ji, J.F., 2008. W–Sn–Nb–Ta-bearing granites in the Nanling range and their relationship to metallogenesis. *Geol. J. China Univ.* 14 (4), 459–473 (in Chinese with English abstract).
- Chen, J., Wang, R.C., Zhu, J.C., Lu, J.J., Ma, D.S., 2013. Multiple-aged granitoids and related tungsten-tin mineralization in the Nanling range, South China. *Sci. China Earth Sci.* 56 (12), 2045–2055.
- Chipley, D., Polito, P.A., Kyser, T.K., 2007. Measurement of U–Pb ages of uraninite and davidite by laser ablation-HR-ICP-MS. *Am. Mineral.* 92 (11–12), 1925–1935.
- Christensen, J.N., Halliday, A.N., Leigh, K.E., Randell, R.N., Kesler, S.E., 1995. Direct dating of sulfides by Rb–Sr: a critical test using the Polaris Mississippi Valley-type Zn–Pb deposit. *Geochim. Cosmochim. Acta* 59 (24), 5191–5197.
- Cross, A., Jaireth, S., Rapp, R., Armstrong, R., 2011. Reconnaissance-style EPMA chemical U–Th–Pb dating of uraninite. *Aust. J. Earth Sci.* 58 (6), 675–683.
- Dalrymple, G.B., Alexander, E.C., Lanphere, M.A., Kraker, G.P., 1981. Irradiation of samples for $^{40}\text{Ar}/^{39}\text{Ar}$ dating using the Geological Survey TRIGA reactor. U. S. Geol. Surv., Professional Paper 1176, Washington.
- Du, A.D., He, H.L., Yin, N.W., Zou, X.Q., Sun, Y.L., Sun, D.Z., Chen, S.Z., Qu, W.J., 1993. Direct dating of molybdenites using the Re–Os geochronometer. *Chin. Sci. Bull.* 38 (15), 1319–1320.
- Eichhorn, R., Holl, R., Jagoutz, E., Scharer, U., 1997. Dating scheelite stages: a strontium, neodymium, lead approach from the Felbertal tungsten deposit, Central Alps, Austria. *Geochim. Cosmochim. Acta* 61 (23), 5005–5022.
- Fayek, M., Kyser, T.K., Riciputi, L.R., 2002. U and Pb isotope analysis of uranium minerals by ion microprobe and the geochronology of the McArthur River and Sue Zone uranium deposits, Saskatchewan, Canada. *Can. Mineral.* 40, 1553–1569.
- Feng, C.Y., Zeng, Z.L., Zhang, D.Q., Qu, W.J., Du, A.D., Li, D.X., She, H.Q., 2011. SHRIMP zircon U–Pb and molybdenite Re–Os isotopic dating of the tungsten deposits in the Tianmenshan-Hongtaoling W–Sn orefield, southern Jiangxi Province, China, and geological implications. *Ore Geol. Rev.* 43 (1), 8–25.
- Gao, B., Xue, C., Chi, G., Li, C., Qu, W., Du, A., Li, Z., Gu, H., 2012. Re–Os dating of bitumen in the giant Jinding Zn–Pb deposit, Yunnan and its geological significance. *Acta Petrol. Sin.* 28 (5), 1561–1567.
- Goldstein, R.H., Reynolds, T.J., 1994. Systematics of fluid inclusions in diagenetic minerals. In: *Sepp Short Course, 31. Sedimentary Geology, Society for (199 pp)*.
- Gulson, B.L., Jones, M.T., 1992. Cassiterite: potential for direct dating of mineral deposits and a precise age for the Bushveld complex granites. *Geology* 20 (4), 355–358.
- Günther, D., Audétat, A., Frischknecht, R., Heinrich, C.A., 1998. Quantitative analysis of major, minor and trace elements in fluid inclusions using laser ablation inductively coupled plasma mass spectrometry. *J. Anal. At. Spectrom.* 13 (4), 263–270.
- Guo, W.K., Zeng, Q.D., Guo, Y.P., Wang, Y.B., Zhang, B., 2018. Rb–Sr dating of sphalerite and S–Pb isotopic studies of the Xinxing crypto-explosive breccia Pb–Zn (Ag) deposit in the southeastern segment of the Lesser Xing'an Zhangguangcai metallogenic belt, NE China. *Ore Geol. Rev.* 99, 75–85.
- Hall, D.L., Sterner, S.M., Bodnar, R.J., 1988. Freezing-point depression of NaCl–KCl–H₂O solutions. *Econ. Geol.* 83 (1), 197–202.
- Harrison, T.M., Heizler, M.T., Lovera, O.M., 1993. In vacuo crushing experiments and k-feldspar thermochronometry. *Earth Planet. Sci. Lett.* 117 (1–2), 169–180.
- Harrison, T.M., Heizler, M.T., Lovera, O.M., Chen, W.J., Grove, M., 1994. A chlorine disinfectant for excess argon released from K-feldspar during step heating. *Earth Planet. Sci. Lett.* 123 (1–4), 95–104.
- He, Z.Y., Xu, X.S., Zou, H.B., Wang, X.D., Yu, Y., 2010. Geochronology, petrogenesis and metallogeny of Piaotang granitoids in the tungsten deposit region of South China. *Geochim. J.* 44 (4), 299–313.
- He, L.Y., Qiu, H.N., Shi, H.S., Zhu, J.Z., Bai, X.J., Yun, J.B., 2016. A novel purification technique for noble gas isotope analyses of authigenic minerals. *Sci. China Earth Sci.* 59 (1), 111–117.
- Heinrich, C.A., Günther, D., Audétat, A., Ulrich, T., Frischknecht, R., 1999. Metal fractionation between magmatic brine and vapor, determined by microanalysis of fluid inclusions. *Geology* 27 (8), 755–758.
- Hu, R.Z., Zhou, M.F., 2012. Multiple Mesozoic mineralization events in South China – an introduction to the thematic issue. *Mineral. Deposita* 47 (6), 579–588.
- Hu, R.G., Wijbrans, J.R., Brouwer, F.M., Wang, M., Zhao, L.H., Qiu, H.N., 2016. $^{40}\text{Ar}/^{39}\text{Ar}$ thermochronological constraints on the retrogression and exhumation of ultra-high pressure (UHP) metamorphic rocks from Xitieshan terrane, North Qaidam, China. *Gondwana Res.* 36, 157–175.
- Hua, R.M., Chen, P.R., Zhang, W.L., Lu, J.J., 2005. Three major metallogenic events in Mesozoic in South China. *Mineral Deposits* 24 (2), 99–107 (in Chinese with English abstract).
- Jiang, S.Y., Slack, J.F., Palmer, M.R., 2000. Sm–Nd dating of the giant Sullivan Pb–Zn–Ag deposit, British Columbia. *Geology* 28 (8), 751–754.
- Jiang, Y.D., Qiu, H.N., Xu, Y.G., 2012. Hydrothermal fluids, argon isotopes and mineralization ages of the Fankou Pb–Zn deposit in south China: insights from sphalerite $^{40}\text{Ar}/^{39}\text{Ar}$ progressive crushing. *Geochim. Cosmochim. Acta* 84, 369–379.
- Kelley, S., 2002. Excess argon in K–Ar and Ar–Ar geochronology. *Chem. Geol.* 188 (1–2), 1–22.
- Kelley, S., Turner, G., Butterfield, A.W., Shepherd, T.J., 1986. The source and significance of argon isotopes in fluid inclusions from areas of mineralization. *Earth Planet. Sci. Lett.* 79 (3–4), 303–318.
- Kempe, U., Belyatsky, B.V., Krymsky, R.S., Kremenetsky, A.A., Ivanov, P.A., 2001. Sm–Nd and Sr isotope systematics of scheelite from the giant Au–(W) deposit Muruntau (Uzbekistan): implications for the age and sources of Au mineralization. *Mineral. Deposita* 36 (5), 379–392.
- Kendrick, M.A., Burgess, R., Patrick, R.A.D., Turner, P.G., 2001. Halogen and Ar–Ar age determinations of inclusions within quartz veins from porphyry copper deposits using complementary noble gas extraction techniques. *Chem. Geol.* 177 (3–4), 351–370.
- Kendrick, M.A., Miller, J.M., Phillips, D., 2006. Part II. Evaluation of ^{40}Ar – ^{39}Ar quartz ages: Implications for fluid inclusion retentivity and determination of initial $^{40}\text{Ar}/^{36}\text{Ar}$ values in Proterozoic samples. *Geochim. Cosmochim. Acta* 70 (10), 2562–2576.
- Koppers, A.A.P., 2002. ArArCALC — software for $^{40}\text{Ar}/^{39}\text{Ar}$ age calculations. *Comput. Geosci.* 28 (5), 605–619.
- Lee, J.Y., Marti, K., Severinghaus, J.P., Kawamura, K., Yoo, H.S., Lee, J.B., Kim, J.S., 2006. A redetermination of the isotopic abundances of atmospheric Ar. *Geochim. Cosmochim. Acta* 70 (17), 4507–4512.
- Li, Q.L., Chen, F.k., Yang, J.H., Fan, H.R., 2008. Single grain pyrite Rb–Sr dating of the Linglong gold deposit, eastern China. *Ore Geol. Rev.* 34 (3), 263–270.
- Li, C.Y., Zhang, R.Q., Ding, X., Ling, M.X., Fan, W.M., Sun, W.D., 2016. Dating cassiterite using laser ablation ICP-MS. *Ore Geol. Rev.* 72, Part 1, 313–322.
- Li, W.S., Ni, P., Pan, J.Y., Wang, G.G., Chen, L.L., Yang, Y.L., Ding, J.Y., 2018. Fluid inclusion characteristics as an indicator for tungsten mineralization in the Mesozoic Yaogangxian tungsten deposit, central Nanling district, South China. *J. Geochem. Explor.* 192, 1–17.
- Liang, X.Q., Dong, C.G., Jiang, Y., Wu, S.C., Zhou, Y., Zhu, H.F., Fu, J.G., Wang, C., Shan, Y.H., 2016. Zircon U–Pb, molybdenite Re–Os and muscovite Ar–Ar isotopic dating of the Xitian W–Sn polymetallic deposit, eastern Hunan Province. *South China and its geological significance. Ore Geol. Rev.* 78, 85–100.
- Liao, X.A., 2017. The Research on Fluid Inclusions of the Zuoba Greisen Type Tungsten Deposit in Southern Jiangxi. East China University of Technology, MSc Thesis (in Chinese with English abstract, 58 pp).
- Lindaas, S.E., Kulis, J., Campbell, A.R., 2002. Near-infrared observation and microthermometry of pyrite-hosted fluid inclusions. *Econ. Geol. Bull. Soc. Econ. Geol.* 97 (3), 603–618.
- Liu, N., Yu, C., 2011. Analysis of onset and development of ore formation in Dajishan tungsten ore area, Jiangxi Province. *China. J. Earth Sci.* 22 (1), 67–74.
- Liu, Y., Deng, J., Li, C.F., Shi, G.H., Zheng, A.L., 2007. REE composition in scheelite and scheelite Sm–Nd dating for the Xuebaoding W–Sn–Be deposit in Sichuan. *Chin. Sci. Bull.* 52 (18), 2543–2550.
- Liu, Z.Q., Mei, L.F., Qiu, H.N., Shen, C.B., Tang, J.G., Yun, J.B., 2011. $^{40}\text{Ar}/^{39}\text{Ar}$ geochronology constraints on hydrocarbon accumulation and destruction periods in the Bankeng paleo-reservoir in the southern margin of the middle Yangtze block. *Chin. Sci. Bull.* 56 (26), 2803–2812.
- Liu, Y., Cheng, Q., Xia, Q., Wang, X., 2014. Mineral potential mapping for tungsten polymetallic deposits in the Nanling metallogenic belt. *South China. J. Earth Sci.* 25 (4), 689–700.
- Liu, J., Wu, G., Qiu, H.N., Li, Y., 2015. $^{40}\text{Ar}/^{39}\text{Ar}$ dating, fluid inclusions and S–Pb isotope systematics of the Shabaosi gold deposit, Heilongjiang Province. *China. Geol. J.* 50 (5), 592–606.
- Lüders, V., 1996. Contribution of infrared microscopy to fluid inclusion studies in some opaque minerals (wolframite, stibnite, bournonite): metallogenic implications. *Econ. Geol. Bull. Soc. Econ. Geol.* 91 (8), 1462–1468.
- Maas, R., McCulloch, M.T., Campbell, I.H., 1986. Sm–Nd and Rb–Sr dating of an Archean massive sulfide deposit: Kidd-creek, Ontario. *Geology* 14 (7), 585–588.
- Mao, J.W., Xie, G.Q., Li, X.F., Zhang, C.Q., Mei, Y.X., 2004. Mesozoic large scale mineralization and multiple lithospheric extension in south China. *Earth Sci. Front.* 11 (1), 45–55 (in Chinese with English abstract).
- Mao, J.W., Xie, G.Q., Li, X.F., Zhang, C.Q., Wang, Y.T., 2006. Mesozoic large-scale mineralization and multiple lithospheric extensions in South China. *Acta Geol. Sin.-Engl. Ed.* 80 (3), 420–431.
- Mao, J.W., Xie, G.Q., Guo, C.L., Chen, Y.C., 2007. Large-scale tungsten-tin mineralization in the Nanling region, south China: metallogenic ages and corresponding geodynamic processes. *Acta Petrol. Sin.* 23 (10), 2329–2338.
- Mao, J.W., Cheng, Y.B., Chen, M.H., Franco, P., 2013. Major types and time-space distribution of Mesozoic ore deposits in South China and their geodynamic settings. *Mineral. Deposita* 48 (3), 267–294.
- McCandless, T.E., Ruiz, J., Campbell, A.R., 1993. Rhenium behavior in molybdenite in

- hypogene and near-surface environments - implications for Re–Os geochronometry. *Geochim. Cosmochim. Acta* 57 (4), 889–905.
- McDougall, I., Harrison, T.M., 1999. *Geochronology and Thermochronology by the $^{40}\text{Ar}/^{39}\text{Ar}$ Method*, 2nd edition. Oxford University Press, New York.
- Merrihue, C., Turner, G., 1966. Potassium-argon dating by activation with fast neutrons. *J. Geophys. Res.* 71 (11), 2852–2857.
- Mitchell, J.G., 1968. The argon-40/argon-39 method for potassium-argon age determination. *Geochim. Cosmochim. Acta* 32 (7), 781–790.
- Morelli, R.M., Creaser, R.A., Selby, D., Kelley, K.D., Leach, D.L., King, A.R., 2004. Re–Os sulfide geochronology of the Red Dog sediment-hosted Zn–Pb–Ag deposit, Brooks Range, Alaska. *Econ. Geol.* 99 (7), 1569–1576.
- Moritz, R., 2006. Fluid salinities obtained by infrared microthermometry of opaque minerals: Implications for ore deposit modeling — A note of caution. *J. Geochem. Explor.* 89 (1–3), 284–287.
- Nakai, S., Halliday, A.N., Kesler, S.E., Jones, H.D., 1990. Rb–Sr dating of sphalerites from Tennessee and the genesis of Mississippi Valley type ore-deposits. *Nature* 346 (6282), 354–357.
- Nakai, S., Halliday, A.N., Kesler, S.E., Jones, H.D., Kyle, J.R., Lane, T.E., 1993. Rb–Sr dating of sphalerites from Mississippi Valley-type (MVT) ore-deposits. *Geochim. Cosmochim. Acta* 57 (2), 417–427.
- Ni, P., Wang, X.D., Wang, G.G., Huang, J.B., Pan, J.Y., Wang, T.G., 2015. An infrared microthermometric study of fluid inclusions in coexisting quartz and wolframite from Late Mesozoic tungsten deposits in the Gannan metallogenic belt. *South China. Ore Geol. Rev.* 65, 1062–1077.
- Onstott, T.C., Phillips, D., Pringlegoodell, L., 1991. Laser microprobe measurement of chlorine and argon zonation in biotite. *Chem. Geol.* 90 (1–2), 145–168.
- Ostendorf, J., Henjes-Kunst, F., Schneider, J., Melcher, F., Gutzmer, J., 2017. Genesis of the carbonate-hosted Tres Marias Zn–Pb–(Ge) deposit, Mexico: constraints from Rb–Sr sphalerite geochronology and Pb isotopes. *Econ. Geol.* 112 (5), 1075–1087.
- Peng, J.T., Hu, R.H., Zhao, J.H., Fu, Y.Z., Lin, Y.X., 2003. Scheelite Sm–Nd dating and quartz Ar–Ar dating for Woxi Au–Sb–W deposit, western Hunan. *Chin. Sci. Bull.* 48 (23), 2640–2646.
- Qiu, H.N., 1996. ^{40}Ar – ^{39}Ar dating of the quartz samples from two mineral deposits in western Yunnan (SW China) by crushing in vacuum. *Chem. Geol. (Isot. Geosci. Sect.)*, 127 (1–3), 211–222.
- Qiu, H.N., Dai, T.M., 1989. $^{40}\text{Ar}/^{39}\text{Ar}$ techniques for dating the fluid inclusions of quartz from a hydrothermal deposit. *Chin. Sci. Bull.* 34 (22), 1887–1890.
- Qiu, H.N., Jiang, Y.D., 2007. Sphalerite $^{40}\text{Ar}/^{39}\text{Ar}$ progressive crushing and stepwise heating techniques. *Earth Planet. Sci. Lett.* 256 (1–2), 224–232.
- Qiu, H.N., Wijbrans, J.R., 2006. Paleozoic ages and excess ^{40}Ar in garnets from the Bixiling eclogite in Dabieshan, China: new insights from $^{40}\text{Ar}/^{39}\text{Ar}$ dating by stepwise crushing. *Geochim. Cosmochim. Acta* 70 (9), 2354–2370.
- Qiu, H.N., Wijbrans, J.R., 2008. The Paleozoic metamorphic history of the Central Orogenic Belt of China from $^{40}\text{Ar}/^{39}\text{Ar}$ geochronology of eclogite garnet fluid inclusions. *Earth Planet. Sci. Lett.* 268 (3–4), 501–514.
- Qiu, H.N., Zhu, B., Sun, D., 2002. Age significance interpreted from ^{40}Ar – ^{39}Ar dating of quartz samples from the Dongchuan copper deposits, Yunnan, SW China, by crushing and heating. *Geochem. J.* 36 (5), 475–491.
- Qiu, H.N., Wu, H.Y., Yun, J.B., Feng, Z.H., Xu, Y.G., Mei, L.F., Wijbrans, J.R., 2011. High-precision $^{40}\text{Ar}/^{39}\text{Ar}$ age of the gas emplacement into the Songliao Basin. *Geology* 39 (5), 451–454.
- Rama, S.N.I., Hart, S.R., Roedder, E., 1965. Excess radiogenic argon in fluid inclusions. *J. Geophys. Res.* 70 (2), 509–511.
- Richards, J.P., Cumming, G.L., Krstic, D., Wagner, P.A., Spooner, E.T.C., 1988. Pb isotope constraints on the age of sulfide ore deposition and U–Pb age of late uraninite veining at the Musoshi Stratiform copper-deposit, central African Copper Belt. *Zaire. Econ. Geol.* 83 (4), 724–741.
- Roddick, J.C., 1983. High precision intercalibration of ^{40}Ar – ^{39}Ar standards. *Geochim. Cosmochim. Acta* 47 (5), 887–898.
- Selby, D., Creaser, R.A., 2005. Direct radiometric dating of hydrocarbon deposits using rhenium–osmium isotopes. *Science* 308 (5726), 1293–1295.
- Shepherd, T.J., Darbyshire, D.P.F., 1981. Fluid inclusion Rb–Sr isochrons for dating mineral deposits. *Nature* 290 (5807), 578–579.
- Sumino, H., Dobrzhenetskaya, L.F., Burgess, R., Kagi, H., 2011. Deep-mantle-derived noble gases in metamorphic diamonds from the Kokchetav massif. *Kazakhstan. Earth Planet. Sci. Lett.* 307 (3–4), 439–449.
- Suzuki, K., Kato, T., 2008. CHIME dating of monazite, xenotime, zircon and polycrase: protocol, pitfalls and chemical criterion of possibly discordant age data. *Gondwana Res.* 14 (4), 569–586.
- Suzuki, K., Qilu, Shimizu, H., Masuda, A., 1993. Reliable Re–Os age for molybdenite. *Geochim. Cosmochim. Acta* 57 (7), 1625–1628.
- Tretbar, D.R., Arehart, G.B., Christensen, J.N., 2000. Dating gold deposition in a Carlin-type gold deposit using Rb/Sr methods on the mineral galkhaite. *Geology* 28 (10), 947–950.
- Turner, G., 1971a. ^{40}Ar – ^{39}Ar ages from the lunar maria. *Earth Planet. Sci. Lett.* 11 (3), 169–191.
- Turner, G., 1971b. Argon 40-argon 39 dating: the optimization of irradiation parameters. *Earth Planet. Sci. Lett.* 10 (2), 227–234.
- Turner, G., 1988. Hydrothermal fluids and argon isotopes in quartz veins and cherts. *Geochim. Cosmochim. Acta* 52 (6), 1443–1448.
- Turner, G., Bannon, M.P., 1992. Argon isotope geochemistry of inclusion fluids from granite-associated mineral veins in southwest and northeast England. *Geochim. Cosmochim. Acta* 56 (1), 227–243.
- Turner, G., Wang, S.S., 1992. Excess argon, crustal fluids and apparent isochrons from crushing K-feldspar. *Earth Planet. Sci. Lett.* 110 (1–4), 193–211.
- Turner, G., Burnard, P., Ford, J.L., Gilmour, J.D., Lyon, I.C., Stuart, F.M., 1993. Tracing fluid sources and interactions. *Philos. Trans. R. Soc. Lond. Ser. A-Math. Phys. Eng. Sci.* 344 (1670), 127–140.
- Wang, S.S., 1983. Age determinations of $^{40}\text{Ar}/^{40}\text{K}$, $^{40}\text{Ar}/^{39}\text{Ar}$ and radiogenic ^{40}Ar released characteristics on K–Ar geostandards of China. *Scientia Geologica Sinica* (4), 315–323 (in Chinese, with English abstract).
- Wang, X.D., Ni, P., Jiang, S.Y., Zhao, K.D., Wang, T.G., 2010. Origin of ore-forming fluid in the Piaotang tungsten deposit in Jiangxi Province: evidence from helium and argon isotopes. *Chin. Sci. Bull.* 55 (7), 628–634.
- Wang, X., Chen, J., Ren, M., 2016. Hydrothermal zircon geochronology: Age constraint on Nanling range tungsten mineralization (Southeast China). *Ore Geol. Rev.* 74, 63–75.
- Wu, Z.C., Liu, J.S., Shu, G.W., Wang, W., Ma, H.Y., 2010. The relationship between yanshanian tectonic-magmatic thermal event and tin-tungsten mineralization at Xitian Nanling area. *Contributions to Geology and Mineral Resources Research* 25 (3), 201–205 (in Chinese with English abstract).
- Xiao, M., Qiu, H.N., Jiang, Y.D., Cai, Y., Bai, X.J., Zhang, W.F., Liu, M., Qin, C.J., 2019. Gas release systematics of mineral-hosted fluid inclusions during stepwise crushing: implications for $^{40}\text{Ar}/^{39}\text{Ar}$ geochronology of hydrothermal fluids. *Geochim. Cosmochim. Acta* 251, 36–55.
- Xiong, S.F., Gong, Y.J., Jiang, S.Y., Zhang, X.J., Li, Q., Zeng, G.P., 2018. Ore genesis of the Wusihe carbonate-hosted Zn–Pb deposit in the Dadu River Valley district, Yangtze Block, SW China: evidence from ore geology, S–Pb isotopes, and sphalerite Rb–Sr dating. *Mineral. Deposita* 53 (7), 967–979.
- Xu, B., Jiang, S.Y., Luo, L., 2015. LA-MC-ICP-MS U–Pb dating of cassiterite from the Jianfengpo Sn deposit in the Pengshan Sn-polymetallic ore field, Jiangxi Province and its geological significance. *Acta Petrol. Sin.* 31 (3), 701–708.
- Yang, J.H., Zhou, X.H., 2001. Rb–Sr, Sm–Nd, and Pb isotope systematics of pyrite: Implications for the age and genesis of lode gold deposits. *Geology* 29 (8), 711–714.
- Yuan, S.D., Peng, J.T., Hu, R.Z., Li, H.M., Shen, N.P., Zhang, D.L., 2008. A precise U–Pb age on cassiterite from the Xianghualing tin-polymetallic deposit (Hunan, South China). *Mineral. Deposita* 43 (4), 375–382.
- Yuan, S.D., Peng, J.T., Hao, S., Li, H.M., Geng, J.Z., Zhang, D.L., 2011. In situ LA-MC-ICP-MS and ID-TIMS U–Pb geochronology of cassiterite in the giant Furong tin deposit, Hunan Province. *South China: New constraints on the timing of tin-polymetallic mineralization. Ore Geol. Rev.* 43 (1), 235–242.
- Yun, J.B., Wu, H.Y., Feng, Z.H., Mei, L.F., Qiu, H.N., 2010. CO_2 gas emplacement age in the Songliao Basin: insight from volcanic quartz ^{40}Ar – ^{39}Ar stepwise crushing. *Chin. Sci. Bull.* 55 (17), 1795–1799.
- Zhang, W.L., Hua, R.M., Wang, R.C., Li, H.M., Qu, W.J., Ji, J.Q., 2009. New Dating of the Piaotang Granite and Related Tungsten Mineralization in Southern Jiangxi. *Acta Geol. Sin.* 83 (5), 659–670.
- Zhang, R.Q., Lehmann, B., Seltmann, R., Sun, W.D., Li, C.Y., 2017a. Cassiterite U–Pb geochronology constrains magmatic-hydrothermal evolution in complex evolved granite systems: the classic Erzgebirge tin province (Saxony and Bohemia). *Geology* 45 (12), 1095–1098.
- Zhang, R.Q., Lu, J.J., Lehmann, B., Li, C.Y., Li, G.L., Zhang, L.P., Guo, J., Sun, W.D., 2017b. Combined zircon and cassiterite U–Pb dating of the Piaotang granite-related tungsten-tin deposit, southern Jiangxi tungsten district. *China. Ore Geol. Rev.* 82, 268–284.
- Zhao, X.F., Zhou, M.F., Li, J.W., Selby, D., Li, X.H., Qi, L., 2013. Sulfide Re–Os and Rb–Sr isotope dating of the Kangdian IOCG metallogenic province, Southwest China: implications for regional metallogenesis. *Econ. Geol.* 108 (6), 1489–1498.